Large Eddy Simulations of Turbulent Heat Transfer in Packed Bed Energy Storage Systems

Large Eddy Simulations of Turbulent Heat Transfer in Packed Bed Energy Storage Systems

Mohammad Jadidi[1], Hanieh Khalili Param[2], Alistair Revell[1], Yasser Mahmoudi[1*]

[1]Department of Mechanical, Aerospace and Civil Engineering (MACE), University of Manchester, M13 9PL, UK
[2]Department of Mechanical, Automotive and Material Engineering (MAME), University of Windsor, N9B 3P4, Canada

[*]Corresponding author: yasser.mahmoudilarimi@manchester.ac.uk

Abstract

The present paper aims to study the effect of partial blocking and flow regime on the mutual turbulent interplay between porous and non-porous regions in packed bed energy storage systems (PBESSs). To this end, high-fidelity pore-scale large eddy simulations (LES) are conducted for two PBESS configurations, namely full blockage and partial blockage under the discharge process at three Re numbers 3600, 7200, and 14400. The influences of the flow major features, including flow channelling and leakage, on the rate of heat transfer (Nusselt number) and pressure drop are investigated for various flow Reynolds (Re) numbers. Results demonstrate that the channelling effect inside the porous region strongly affects the temperature profiles and leads to local maximum peaks of Nusselt (Nu) number on the upper and lower sides of pore elements. For the partial blockage, it is observed that 79% of the flow entering the porous block leaks from the porous region into the non-porous region through the porous-fluid interface at Re=3600, which reduces by 26% as the Re increases to 14400. The flow leakage leads to the formation of counter-rotating vortex pair structures inside and over the porous block. It also causes local maximum peaks of Nu number at the lower sides of pore elements and changes the stagnation points' position at the leading edge of the porous block near the porous-fluid interface. Compared to the full blockage configuration, temperature profiles inside the porous block are less dependent on the Re number for the partial blockage case. Finally, the pressure drag force for the full blockage is about 21.4 and 30.9 times that of partial blockage at Re=3600 and 14400, respectively. Whereas at these Re numbers, the average Nu number for the full blockage is nearly 51.2% and 57.3% higher than that of the partial blockage. Consequently, blocking the entire fluid flow area may not necessarily be the best design, since it may result in excessive pressure drops without significant heat transfer enhancement.

Keywords: Porous flow; Packed bed energy storage systems; Flow leakage; Pore-scale large eddy simulations; Nusselt number; Pressure drag.

Nomenclature

variable	Meaning	Unit
C_D	Pressure coefficient	–
dA	Differential surface area on the pore element	m^2
D	Distance between the centres of two consecutive pore elements	m
F_D	Drag force	N
F_L	Lift force	N
$F_{\tau X}$	Skin friction force in the flow streamwise direction	N
$F_{\tau Y}$	Skin friction force in the flow vertical direction	N
h	Height of the porous block	m
H	Channel height	m
k	Turbulence kinetic energy	m^2/s^2
k_f	Thermal conductivity of the working fluid	W/m.K
L	Length of the porous block	m
p	Pressure	Pa
q_{wall}	Heat flux on the wall	W
Q	Second invariant of velocity gradient tensor	$1/s^2$
Q_{in}	Flow rate that enters the porous block from the windward face	m^3/s
Q_{leak}	Flow rate that leaks across the porous-fluid interface to non-porous region	m^3/s
$Re=UH/\upsilon$	Reynolds number based on the inlet bulk velocity and channel height	–
$\bar{S}_{ij}$	Resolved strain rate tensor	1/s
t	Time	s
$t^* = t \times U/D$	Non-dimensional time unit	–
T	Temperature	K
Δt	Time step	s
u_i'	Velocity fluctuation in i[th] direction, $u_i' = \bar{u}_i - < \bar{u}_i >$	m/s
u	Streamwise velocity component	m/s
U	Inlet bulk velocity	m/s
v	Vertical velocity component	m/s
X	Streamwise direction	m
Y	Vertical direction	m
$\widetilde{\Delta Y}$	Mean cell size in the vertical direction	m
Z	Spanwise (Lateral) direction	m
Symbol		
β	Angle of the connecting line between the stagnation point and the centre of the pore element with regard to the horizontal direction	degree
Δ	Filter width	m
$\theta = \dfrac{T - T_{inlet}}{T_{wall} - T_{inlet}}$	Non-dimensional temperature	–
λ	Integral length scale	–
υ	Molecular kinematic viscosity	m^2/s
υ_{SGS}	Sub-grid scale eddy viscosity	m^2/s
ρ	Density	kg/m^3
τ_{ij}	Sub-grid scale (SGS) turbulent stress tensor	m/s^2
Φ	Porosity	–
Ω_{ij}	Rotation rate tensor	1/s
$\langle \ \rangle$	Time-averaged value	–
Subscript		
D	Drag	
L	Lift	
full	Full blockage	
in	Inlet	

loc	local	
Num	Numerical	
Partial	Partial blockage	
res	Resolved	
RMS	Root mean square	
s	Surface of pore element	
SGS	Sub-grid scale	
τ	Skin friction	
$\parallel$	Parallel to the pressure	
$\perp$	Perpendicular to the pressure	
Superscript		
$\overline{}$	Filtration (top hat filter)	
$'$	Fluctuation	
Abbreviation		
AR=L/h	Aspect ratio, i.e., ratio of the porous block's length to its height	−
CFL	Courant–Friedrichs–Lewy number	−
CRVP	Counter-rotating vortex pair	
K-H	Kelvin-Helmholtz	
LES	Large Eddy Simulations	
Nu	Nusselt number	−
PBESS	Packed bed energy storage system	
RANS	Reynolds-Averaged Navier-Stokes	
Re	Reynolds number	−
TKE	Turbulent kinetic energy	m^2/s^2

1 Introduction

Packed bed energy storage systems (PBESSs) are used in numerous applications, including advanced adiabatic compressed air and liquid-air energy storage systems [1, 2], pumped thermal electricity storage [3], and concentrating solar power and geothermal energy [4, 5]. PBESSs store and release thermal energy through heating and cooling fluids, using sensible and latent heat [6, 7]. In PBESSs, a fluid with a higher temperature than solid pore elements passes through the porous medium during the charging process, and pore elements absorb and store energy by exchanging energy between two phases. The discharge process, on the other hand, releases stored energy from hot pore elements into a colder fluid to heat it [7]. Phase change materials (PCMs) have been widely used in PBESSs to enhance thermal performance at charging and discharging processes [8]. However, the main disadvantage of PCMs is their low conductivity which has been addressed by several methodologies, such as fin and metal foam [9, 10], magnetic field and nanoparticles [11, 12].

Heat transfer and pressure drop need to be investigated simultaneously in the PBESSs to reach a trade-off between them [4, 13]. It has been shown that the full blockage of the available flow area is not necessarily the best design as it can lead to unnecessary higher pressure drop and even lower heat transfer rates than partially blocking porous inserts [14]. However, the partial blockage of the flow area adds another unknown to the problem: "momentum and energy exchange across the porous-fluid interface." Although flow and heat transfer through the packed beds have been extensively studied numerically and experimentally [15-18], interface modelling remains a challenging question in the literature. Experiments addressing this issue are, surprisingly, rare [19]. Moreover, the effect of some prominent flow features in PBESSs such as flow leakage and channelling effect on the energy exchange between porous and non-porous regions have not been addressed in the literature yet.

Singh et al. [20] have performed vast experimental studies on PBESSs to develop correlations for the

Nusselt (Nu) number and friction factor as a function of Re number, void fraction, and permeability. Baghapour et al. [13] have performed experimental and modelling investigations on the PBESSs with two porosities, 37.5% and 39%, to calculate the pressure drop, considering the impacts of the inertial forces and Laplacian friction. The proposed semi-analytical correlation covered permeabilities from a low value (like a packed bed with densely arranged spheres) to a high value (a pure viscous fluid flow) [13]. Anuar et al. [19] examined experimentally the effects of the inlet velocity, pore density, and blockage ratio on the pressure drop and flow features in partially filled channel flows containing metal foam blocks. The results demonstrated that at lower blockage ratios (i.e., blockage ratio < 0.1), the pressure drop caused by the metal foam is lower than that of the solid block, measured under the same conditions. Whereas, at higher blockage ratios (> 0.4), the pressure drop of the packed bed is higher than that of the solid block [19]. In other studies, Anuar et al. [21, 22] showed that flow leaks from porous into non-porous regions (flow leakage) at specific pore-density, foam length, and blockage ratios. In addition, the authors emphasized that velocity fluctuations and changes in flow direction at the porous-fluid interface impact the pressure drop remarkably [21].

In addition to experimental investigations, several numerical studies can be found in the literature on PBESSs and porous media [23-26]. Yang et al. [27] utilized packed beds with ellipsoidal/non-uniform or spherical elements for the first time and investigated flow and heat transfer enhancement by RANS models. They showed that an appropriate selection of the packing arrangement and pores' shape could reduce the pressure drop and increase the overall heat transfer significantly. By employing Darcy–Brinkman–Forchheimer model, Mahmoudi and Karimi [28] investigated the heat transfer enhancement in a turbulent channel flow partially filled with a porous medium. Various parameters, including porosity, element diameter, conductivity ratio, and Darcy number (Da) were considered to investigate the reliability of the local thermal equilibrium (LTE) assumption. The authors proposed an optimum porous thickness for increasing heat transfer under varying inertia parameter with acceptable pressure losses [28]. Barbour et al. [1] developed a numerical model for adiabatic compressed air energy storage (A-CAES) and showed that efficiency above 70% is achievable. In 2019, direct numerical simulations (DNS) of convective heat transfer in saturated porous-fluid systems with porosities 56%-89% and Re numbers ranging from 500 to 2000 were carried out by Chu et al. [29]. They revealed that increasing the Re number raises the pressure drop and Nu number. Whereas their further investigation of the ratio of the Stanton number to skin friction (St/C_f) disclosed that increasing the Re number causes more pressure drop than heat transfer enhancement [29]. Very recently, Jadidi et al. [30, 31] conducted large eddy simulations (LES) in a composite porous-fluid system with a blockage ratio of 0.5 at Re=3600, 7200, and 14400. They made special attention to the exchange of the flow (flow leakage) between the non-porous and porous regions at the porous-fluid interface. It was shown that the flow leakage changes the evolution of the hairpin structures over the porous-fluid interface. Also, they showed that increasing the Re number from 3600 to 14400 decreases the flow leakage by 24%.

Despite several numerical studies in the literature for the packed bed energy storage systems (PBESSs), there is still a paucity of pore-scale numerical simulations emphasizing the momentum and energy exchange across the porous-fluid interface. The literature lacks the influence of partial blocking on the interactions between porous and non-porous regions, and local distributions of the Nu number and pressure drop in PBESSs. Hence, the objective of the present paper is to answer the following two questions: (1) What is the impact of the partial blockage and Re number on the flow major features in PBESSs, including flow leakage, flow channelling, and wake region behind the porous block? (2) How do the partial blockage and Re number affect the thermal field in the system, the local distributions of Nu number and the pressure drop? To this end, momentum and energy exchange for two PBESS configurations, namely full blockage and partial blockage, are investigated under the discharge process employing a high-fidelity pore-scale large eddy simulation (LES). The analysis is performed for PBESSs with porosity of 53%, blockage ratios of 0.5 and 1, and aspect ratios of 3.33 and 1.66 at three Re numbers 3600, 7200, and 14400. The range of the Re number is chosen to capture the flow transition from the laminar to the turbulent at the porous-fluid interface. It is the first time that the influence of the flow leakage and channelling effect phenomena on the local variations of the Nu number and pressure loss are addressed at various Re numbers in PBESSs using high-fidelity numerical simulations.

2 Computational methods

2.1 Computational domain and boundary conditions

The computational domain is a channel containing a porous block depicted in **Figure 1** (a, b), with porosity $\Phi = 53\%$ and aspect ratios ($AR = L/h$) of 3.33 and 1.66, representing (partial blockage and full blockage configurations, respectively. The first porous block is a full blockage packed bed made of spheres with diameter D, and the second one is a partial blockage packed bed where the blockage ratio (i.e., ratio of the height of the porous region to the channel height) is $h/H = 0.5$. The computational domain has the dimensions of 70D, 6D, and 5D in the X, Y, and Z directions, respectively. The flow Reynolds (Re) numbers, based on the channel height (H) and inlet velocity (U), are 3600, 7200, and 14400, resulting in 6 cases in the present study. No-slip boundary condition is considered on the solid surfaces in the porous region. Constant wall temperature (T_{wall}) boundary condition (i.e., $\theta = (T - T_{inlet})/(T_{wall} - T_{inlet}) = 1$) is applied on the solid surfaces of the porous region. The non-dimensional temperature at the inlet is equal to zero ($\theta = 0$). The bottom and top boundaries of the channel are assumed adiabatic. **Table 1** summarizes the boundary conditions applied to the computation domain. Also, the description of computational domain details can be found in the recent study by Jadidi et al. [30]. **Figure 1** (c) displays two spanwise locations, namely "trough plane" and "crest plane", where LES results are presented. The crest planes pass through the centres of the spheres, while the trough planes pass through the centres of the connecting bridges (between the spheres). The crest and trough planes can be made in the streamwise direction as well. At trough and crest locations, porous block experiences remarkably different flow physics owing to possessing different permeabilities. The interface on the crest plane is locally impermeable, allowing no flow penetration at this location. Nonetheless, the trough plane has a fully open (permeable) interface, which enables fluid exchange between the surface and subsurface regions. The topology and resolution of the mesh for the pores' surfaces are depicted in **Figure 1** (d).

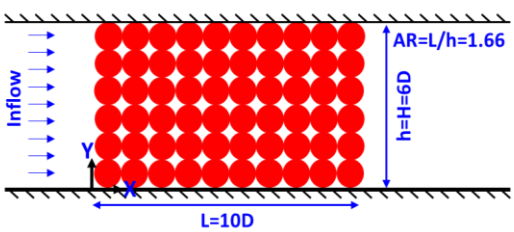

(a) Schematic view of the full blockage of the flow area (blockage ratio=1). The dimensions are not scaled.

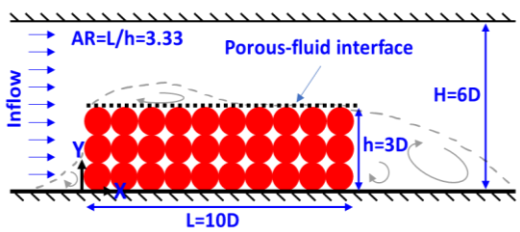

(b) Schematic view of the partial blockage of the flow area (blockage ratio=0.5). The dimensions are not scaled.

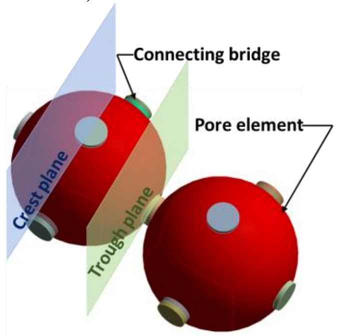

(c) Cubic packed arrangement of spheres (pore elements)

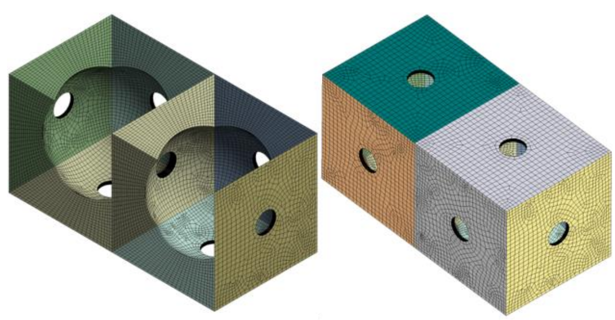

(d) Mesh resolution for pore elements' surfaces

Figure 1 (a) Computational domain for full blockage case; **(b)** Computational domain for partial blockage case; **(c)** Porous block with packed cubic arrangement formed from spheres (bridge method is employed at the contact point of spheres, porosity $\Phi = 53\%$, D=6 mm), and illustration of two "trough plane" and "crest plane" for presenting the results; **(d)** Mesh resolution around the pore elements.

Table 1 Boundary conditions implemented to the computational domain

Inlet boundary	Uniform inlet velocity; U=1, 2 and 4 (m/s) for Re=3600, 7200 and 14400, respectively
Outlet boundary	The gauge pressure is zero; the gradient for all other flow variables is zero.
Side boundaries	Periodic boundary condition.
Top wall, Bottom wall, and pore element walls	No slip.

2.2 Governing equations and numerical methods

By applying a top hat filter to the governing equations of the flow field, the incompressible filtered equations for the resolved fields of the LES approach are derived as follows [32, 33]:

$$\frac{\partial \overline{u_i}}{\partial X_i} = 0 \tag{1}$$

$$\frac{\partial \overline{u_i}}{\partial t} + \frac{\partial}{\partial X_j}(\overline{u_i}\overline{u_j}) = -\frac{1}{\rho}\frac{\partial \bar{p}}{\partial X_i} + \frac{\partial}{\partial X_j}\left(\upsilon \frac{\partial \overline{u_i}}{\partial X_j} - \tau_{ij}\right) \tag{2}$$

$$\frac{\partial \overline{\mathrm{T}}}{\partial t} + \frac{\partial}{\partial X_j}(\overline{\mathrm{T}}\overline{u_j}) = \frac{\partial}{\partial X_j}\left((\alpha + \alpha_{SGS})\frac{\partial \overline{\mathrm{T}}}{\partial X_j}\right) \tag{3}$$

where, $\overline{u_i}$, $\overline{p}$, and $\overline{\mathrm{T}}$ are the filtered velocity in i^{th} direction, pressure, and temperature, respectively. These equations govern the evolution of the large, energy-carrying scales of motion. The effect of the small scales in the flow field appears in a sub-grid scale (SGS) turbulent stress tensor, $\tau_{ij} = \overline{u_i u_j} - \overline{u_i}\,\overline{u_j}$, which is unknown and must be modelled. In the present simulation, the SGS turbulent stress is calculated based on the Boussinesq hypothesis.

$$\tau_{ij} - \frac{1}{3}\tau_{kk}\delta_{ij} = -2\upsilon_{SGS}\,\overline{S_{ij}} = -2C_\tau\,\Delta\,k_{SGS}^{1/2}\,\overline{S_{ij}} \tag{4}$$

where, υ_{SGS} is the SGS turbulent viscosity. In this study, υ_{SGS} is modelled based on the localized dynamic k_{SGS}-equation model [34]. Also, α_{SGS} can be estimated through the sub-grid scale (SGS) Prandtl number, $Pr_{SGS} = \upsilon_{SGS}/\alpha_{SGS}$, which is assumed 0.7 in the present study [35]. u_i' is velocity fluctuation in the i^{th} direction which is defined as $u_i' = \overline{u_i} - <\overline{u_i}>$, where $(\overline{\ldots})$ and <…> refer to the filtration and time-averaging operations.

The filtered governing equations are discretized by implementing the finite volume method (FVM). All the computations are carried out in the open-source object-oriented C^{++} programming in the OpenFOAM CFD package [36]. The second-order central difference scheme is adopted for spatial discretization. The implicit second-order backward difference scheme is used for the time integration. The governing equations are solved using standard pressure–velocity coupling method based on the PIMPLE algorithm [36]. The PIMPLE algorithm is a variation of the PISO method, where outer-correction loops (i.e., cycling over a given time step for several iterations) are employed to maintain the solver's stability, illustrated in a flowchart (**Figure 2**). If no outer corrector loops are used, the algorithm is directly equivalent to the PISO method. In this study, "nOuterCorr" and "nNonOrthoCorr" are considered 2 and 3, respectively [37].

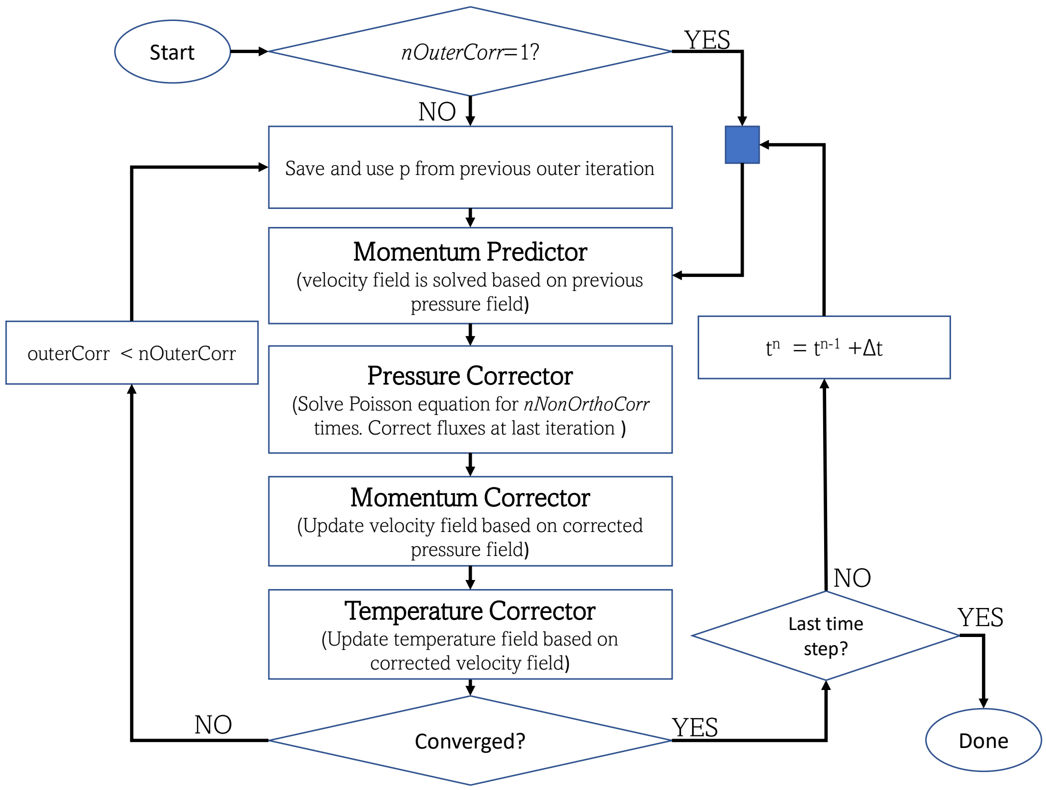

Figure 2 Flowchart of PIMPLE solution procedure used in OpenFOAM. "nOuterCorr" is the number of outer corrector loops, and "nNonOrthoCorr" is the number of non-orthogonal pressure corrector loops.

In order to capture the evolution of the flow features accurately, a physical time step is selected for each grid that keeps the CFL number below unity. The time averaging process is initiated once the initial transient conditions have passed, and a semi-steady state condition is achieved. All the present numerical results are averaged at least for 490 non-dimensional time units ($t^* = t \times U/D$), where U is the flow mean velocity at the channel inlet. The details of the numerical procedure are presented in **Table 2**.

Table 2 Details of the numerical settings

Numerical settings	**Schemes/Methodology**	**Description/Comments**
Pressure-velocity coupling algorithm	PIMPLE algorithm	(Combination of SIMPLE and PISO algorithm)
Time discretization	Backward scheme	Second-order implicit
Convection term discretization	Central differencing scheme	Unbounded second-order
Divergence term discretization	Bounded central difference scheme	Second-order bounded
Laplacian term discretization	Corrected	Unbounded second-order
Time step size	$\Delta t = 10^{-4} \times D/U$	Satisfies the CFL number condition (CFL<1)
Sampling time	$t^* = t \times U/D = 490$	70 flow-through times over the porous block

At Re=3600, the computational domain is approximately discretized into 12.3 million and 10.3 million non-uniform grid cells for full and partial blockage cases, respectively. For higher Re numbers, the computational grids are adapted to maintain the same resolution as Re=3600. For the evaluation of grid resolutions, two-point correlations implemented by Bazdidi-Tehrani et al. [38] are employed. The ratio of integral length scale (λ) to grid spacing is an appropriate method for the evaluation of grid resolution since this ratio demonstrates the number of cells in the resolved largest scale. The ratio of the integral length scale to the mean grid spacing in the vertical direction ($\widetilde{\Delta Y} = L_Y/N_Y$) at the center plane ($Z/D = 0$) at $X/D = 12$ is calculated for 6 cases. It is found that at least six cells have been included in the vertical integral length scale, seeming to be sufficient [39].

2.3 Validation

In order to validate the implemented code in OpenFOAM, the experimental setup of Leu et al. [40] was engaged to perform the LES calculations. The details of the computational domain and boundary conditions utilized for the testbed of Leu et al. [40] can be found in the recent pore-scale LES study of Jadidi et al. [30, 31]. **Figure 3** (a, b) compares the vertical distribution of non-dimensional time-averaged streamwise and vertical velocity components and micro-scale parameter, Reynolds shear stress ($< u'v' >/UU$), against the experimental data [40] at two streamwise locations $X/D = 1.6$ and 3. As shown in the figure, the results are in reasonable agreement with the measured data [40]. In addition, **Figure 3** (c, d) compares the macroscale parameters, pressure drop, and overall Nu number, of the current LES study at three Re numbers with the available references in the literature [41-49]. The LES results reasonably follow the trend of the pressure drop and Nu number variations versus Re numbers compared to the references.

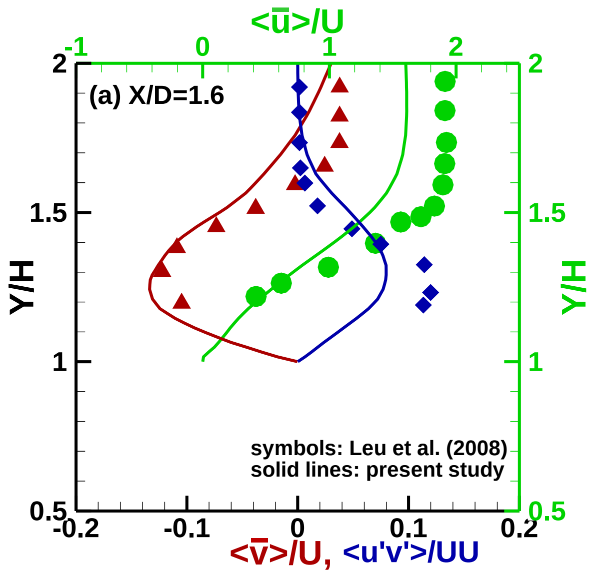

(a) Comparison of present results with the experimental data of Leu et al. [40] at $X/D = 1.6$

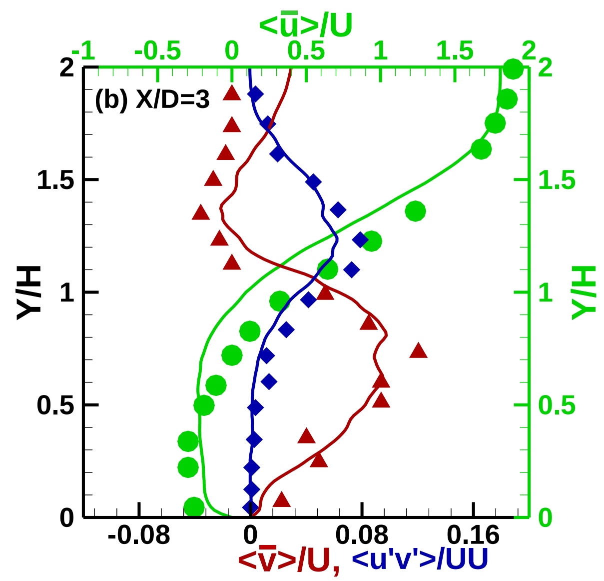

(b) Comparison of present results with the experimental data of Leu et al. [40] at $X/D = 3.0$

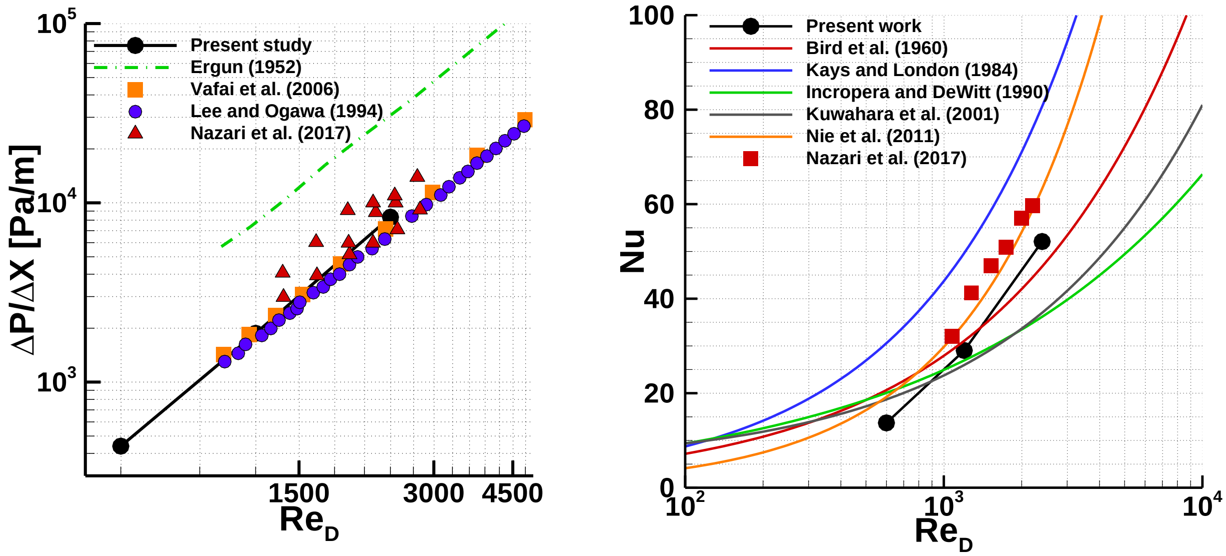

(c) Comparison of pressure drop with different references (d) Comparison of Nu number with different references

Figure 3 (a, b) Vertical distribution of time-averaged streamwise velocity, vertical velocity, and Reynolds shear stress compared with the experimental data of Leu et al. [40] at two locations: (a) $X/D = 1.6$ and (b) $X/D = 3.0$; **(c)** Comparison of Pressure drops in the packed bed with available references: Eurgan (1952) [42], Vafai et al. (2006) [44], Lee and Ogawa (19984) [41], Nazari et al. (2017) [43]; **(d)** Comparison of Nu number with available references: Bird et al. [45], Kays and London [46], Incropera and DeWitt [47], Kuwahara et al. [48], Nie et al. [49], Nazari et al. [50].

3 Discussion of results

Figure 4 displays the vertical distributions of the non-dimensional time-averaged temperature ($<\overline{\Theta}>$) at different streamwise sections, $X/D = 1, 5, 9,$ and 11. When the flow passes through the narrow gaps between the pores, a channelling effect dominates the flow pattern [30, 31], especially for the full-blockage cases. This phenomenon creates streamwise-oriented high-momentum paths in the porous region. Therefore, the temperature profiles exhibit a non-uniform wavy pattern owing to the geometrical characteristics of the pores and correspondingly the channelling effect. As X/D increases from 1 to 11 in **Figure 4** (a-c), the temperature profiles become more uniform for the full blockage cases, especially at Re=7200 and 14400. Similar trends are also observed within the porous region for the partial blockage cases in **Figure 4** (d-f). However, the temperature profiles of partial blockage are less affected by the Re number.

In addition, $<\overline{\Theta}>$ profiles of partial blockage in **Figure 4** (d-f) approach zero at $Y/D \geq 4.6$ ($1.6D$ above the porous-fluid interface). This means that above $Y/D\sim4.6$, the cold flow over the porous block has no interaction with the hot pore elements. Finally, **Figure 4** (f) shows that the vertical distributions of $<\overline{\Theta}>$ are independent of streamwise location after $X/D\sim5$ (see Note 1) for Re=14400. The shear layer above the porous block interacts strongly with the pore elements at Re=14400, enhancing the flow mixing between hot porous and cold non-porous regions which makes the temperature profiles independent of streamwise location.

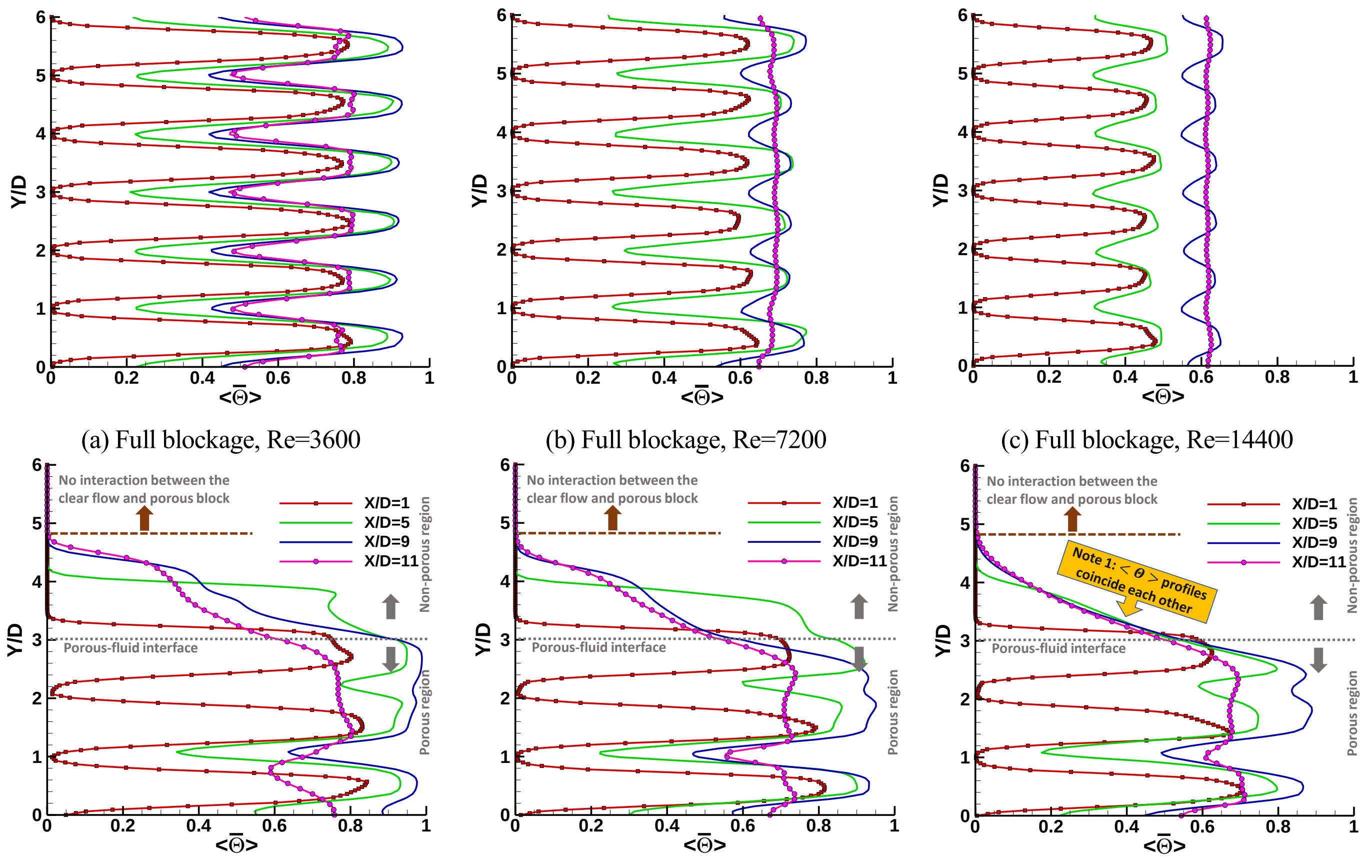

(a) Full blockage, Re=3600 (b) Full blockage, Re=7200 (c) Full blockage, Re=14400

(d) Partial blockage, Re=3600 (e) Partial blockage, Re=7200 (f) Partial blockage, Re=14400

Figure 4 Vertical profiles of the non-dimensional time-averaged temperature ($< \overline{\Theta} >$) at different streamwise locations along the porous block on the trough plane at Re=3600, 7200, and 14400; **(a-c)** Full blockage (blockage ratio = 1.0); **(d-f)** Partial blockage (blockage ratio = 0.5).

Figure 5 displays the positive iso-surface of vertical velocity ($< \overline{v} >/U$) and streamlines for the partial blockage at Re=3600, indicating the flow leakage from the porous into the non-porous regions. They demonstrate that some portion of the fluid entering the porous block is pushed upwards and leaves the porous region into the non-porous region (flow leakage) [30]. Moreover, the streamlines illustrate how the flow leakage clogs the horizontal channel flows beneath the interface and reduces the streamwise momentum of the pore flow.

The time-averaged flow rate that enters the porous block from the windward face is defined as Q_{in}, and the time-averaged flow rate that leaks from the porous-fluid interface to the non-porous region is defined as Q_{leak}. The ratio Q_{leak}/Q_{in} proves that for the partial blockage at Re=3600 more than 79% of the entering flow leaks from the porous-fluid interface through the entire porous length, and this ratio is nearly 65% for the first half of the porous length. The flow leakage is 82% higher in the first half of the porous length compared to the second half. By increasing the Re number from 3600 to 14400, flow leakage decreases from 79% to 58% for the entire porous length and from 65% to 48% for the first half. More information about the flow leakage can be found in [31].

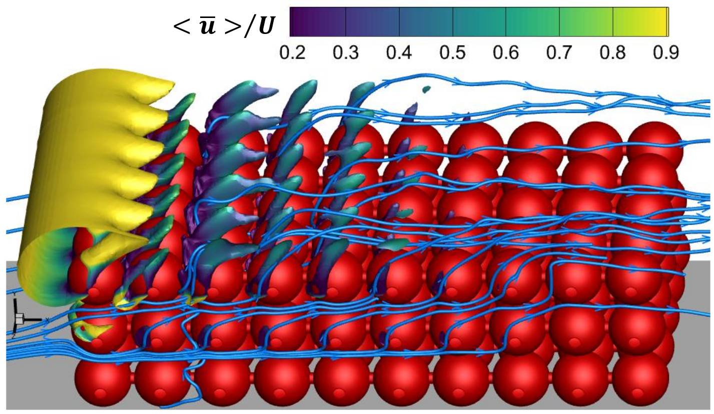

Figure 5 Iso-surface of non-dimensional time-averaged vertical velocity ($< \bar{v} >/U = 0.5$), colored by non-dimensional time-averaged streamwise velocity at Re=3600 for the partial blockage; Streamlines show how the flow leakage clogs the streamwise-oriented flow pattern within the porous block and shortens the channelling effect below the interface.

Figure 6 shows the temperature contours ($< \overline{\Theta} >$) for the full and partial blockages at Re=3600. Also, the figure displays the streamlines, visualized by the line integration convolution (LIC) method [51], and the velocity vectors coloured by the instantaneous temperature on the trough plane ($Z/D = -0.5$). For full blockage, the streamlines around the pore elements clearly illustrate the formation of the channelling effect and stagnation regions. Near the leading edge ($X/D = 2$), the channelling effect causes low-temperature spots (blue areas) which gradually diminish by moving downstream (from $X/D = 2$ to 8) as the incoming flow interacts with the hot pore elements. However, for Re=3600 the channelling effect sustains up to the trailing edge as can be seen in **Figure 6** (a) at $X/D = 8$. This tendency can also be observed in the wavy pattern of temperature profiles at $X/D = 9$ and 11 in **Figure 4** (a).

In **Figure 6** (b), the streamlines at $X/D = 2$ illustrate the generation of counter-rotating vortex pair (CRVP) structures over the porous block, originating from the porous inside (see the zoom view in **Figure 6** (b)). The CRVPs manipulate the momentum and energy exchange between the porous and non-porous regions. The CRVPs expansion is limited by the pore elements inside the porous block, while their growth is unrestricted in the non-porous region. Thus, the CRVPs enlarge freely over the porous block, and their centres are pushed away from the interface as they move downstream. As shown in **Figure 6** (b), the temperature contours above the porous block follow the velocity patterns induced by the CRVPs. For instance, similar to the CRVPs centres along the porous block, the core of the hot regions moves away from the interface toward downstream. Finally, the velocity vectors in **Figure 6** (b) on the trough plane ($Z/D = -0.5$) are indicative of the flow leakage from porous to non-porous regions. Whereas, at the trailing edge, the vectors highlight that some portion of the flow over the porous block, enters the porous region (opposed to the flow leakage).

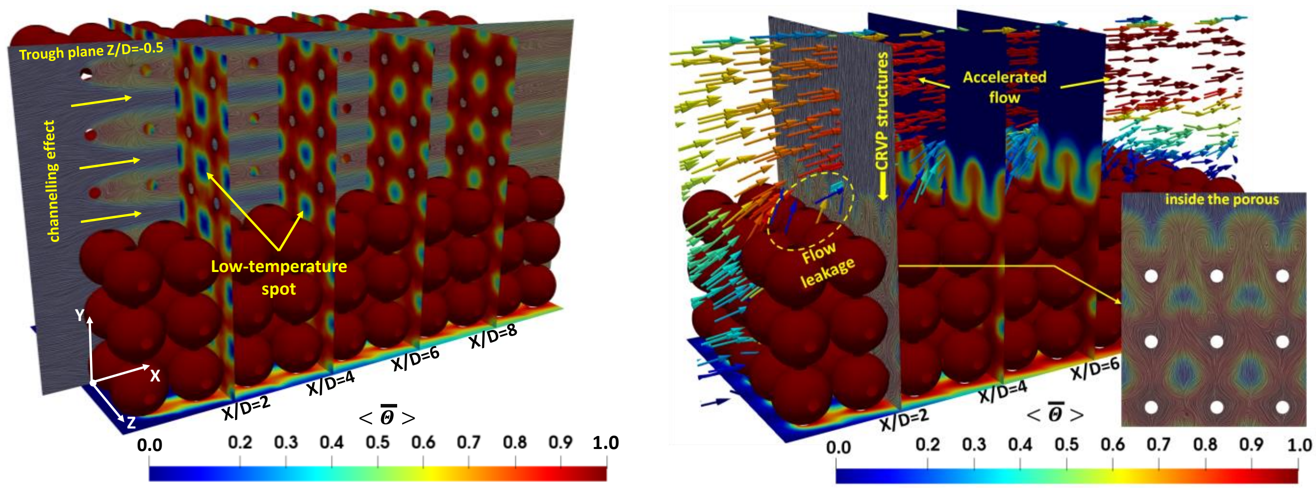

(a) Full blockage, Re=3600

(b) Partial blockage, Re=3600

Figure 6 Contours of non-dimensional time-averaged temperature ($<\bar{\Theta}>$) on the pore elements, the bottom wall under the porous block, and different streamwise planes ($X/D = 2, 4, 6$, and 8) at Re=3600. The streamlines (coloured by temperature) are superimposed on the trough plane $Z/D = -0.5$; **(a)** Full blockage and **(b)** Partial blockage.

The instantaneous temperature ($\overline{\Theta}$) contours on trough and crest planes are depicted in **Figure 7** (a-f) and **Figure 7** (g-l), respectively, for full and partial blockages at three Re numbers. The temperature distributions are quite different for the full and partial blockages. For full blockage in **Figure 7** (a, c, e), the streamwise-oriented channelling effect shows a minor variation along different elevations, while it is non-uniform for the partial blockage in **Figure 7** (b, d, f). In contrast to Re=7200 and 14400, the channelling effect for full blockage at Re=3600 sustains along the porous length, and consequently, the wavy patterns of instantaneous temperature preserve up to nearly $6D$ after the porous block ($X/D = 16$). **Figure 7** (c, e) illustrates that the instantaneous temperature contours of full blockage at Re=7200 and 14400 reach nearly a uniform distribution before $X/D{\sim}12$. For partial blockage in **Figure 7** (b, d, f), the pore flow leaks from the porous into the non-porous regions on the trough planes. The entrainment of high-temperature flows around the pore elements near the leading edge (marked as A in **Figure 7** (b, f)) illustrates the flow direction with an angle of 45^{o} in this region.

Figure 7 (g, i, k) demonstrate that increasing the Re number causes the temperature distribution to become more uniform after the porous block at the crest planes. The temperature contours of the partial blockage in **Figure 7** (h, j, l) show the growth of the shear layer above the porous-fluid interface. The evolution of the shear layer can be characterized by three distinct segments. The first one is characterised by the flow separation at the leading edge of the porous block and the onset growth of the Kelvin-Helmholtz instabilities. As the Re number increases from 3600 to 14400, the first segment's length reduces, and the onset of K-H instabilities shifts upstream. The second segment is identified by the vortex formation and pairing that lead to the rapid growth of the shear layer along the porous length. The third segment is recognized by the cross-interaction of the wake and shear layer at the trailing edge that leads to the deterioration of the rollers. More discussion about the turbulent boundary layer development over the porous-fluid interface can be found in [31].

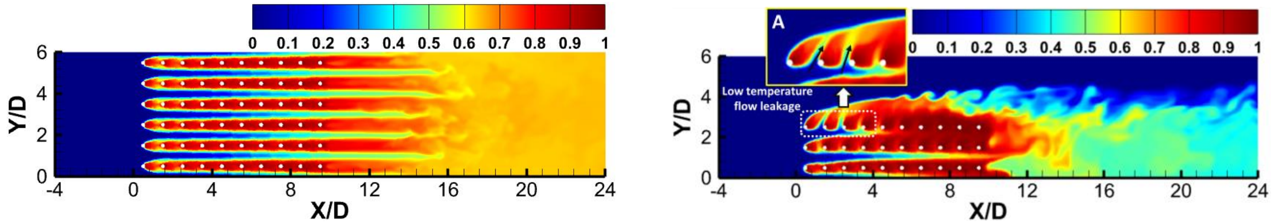

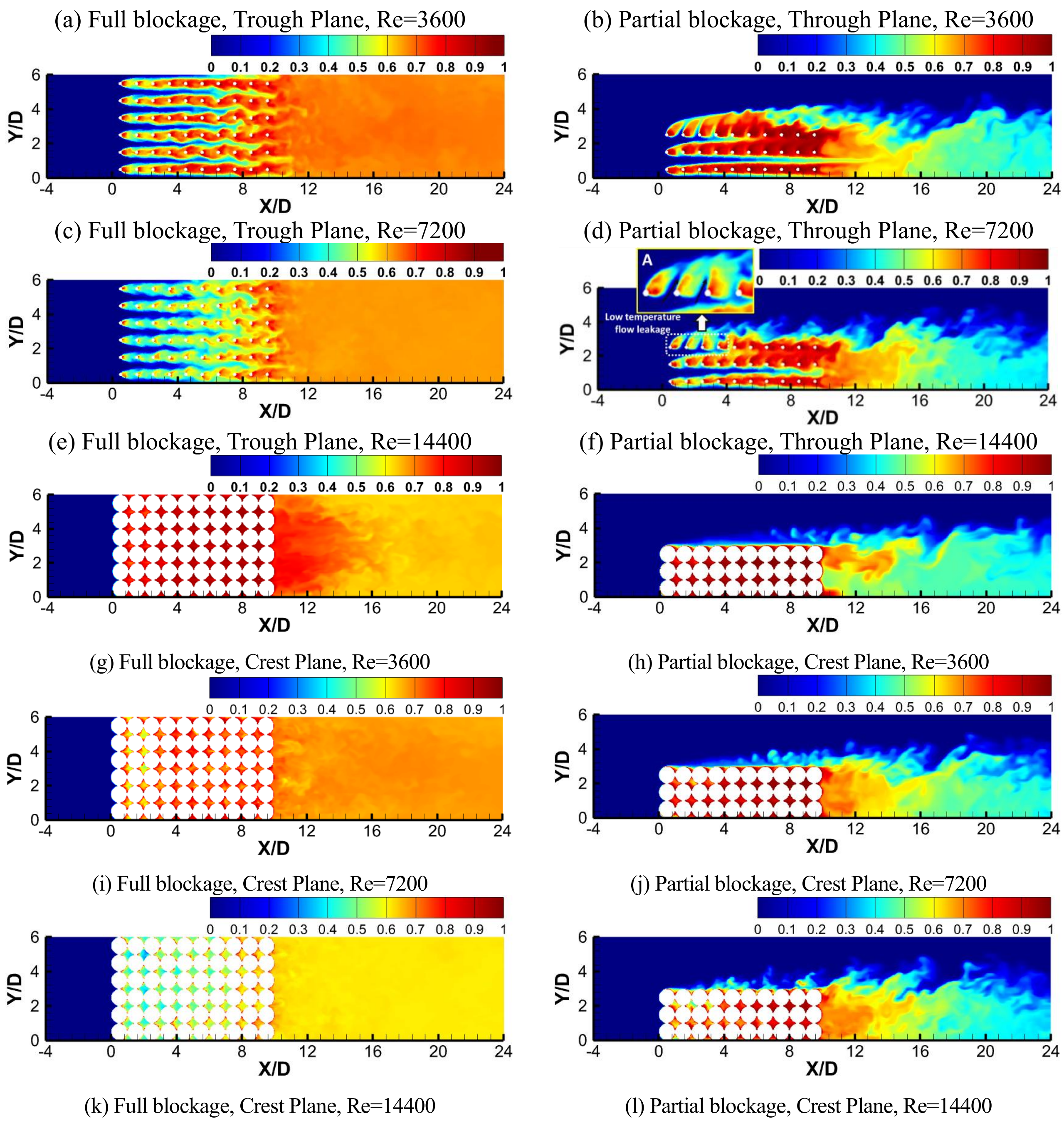

Figure 7 Front view contours of non-dimensional instantaneous temperature ($\overline{\Theta}$) on the trough and crest planes for full and partial blockages at Re=3600, 7200, and 14400; **(a-f)** Trough plane; **(g-l)** Crest plane.

Figure 8 displays the streamwise velocity ($< \bar{u} >/U$), temperature ($< \overline{\Theta} >$), streamwise Reynolds shear stress ($< u'u' >/UU$), and streamwise turbulent heat flux ($< u'T' >/< u'T' >_{max}$) profiles in the wake region. The relevant parameters for each Re number are made non-dimensional by a reference velocity (U) which was used in the definition of that Re number. Thus, the reference velocity is 1, 2, and 4 for Re=3600, 7200, and 14400, respectively. The first visible difference between the full and partial blockages is the non-uniform wavy distribution of parameters across the entire channel height for the full blockage. As shown in **Figure 8** (a, c), the time-averaged velocity and temperature profiles for Re=3600 keep their non-uniform wavy patterns up to $X/D = 13$ ($3D$ after the porous block). In contrast, for Re=7200 and 14400, they reshape toward a uniform distribution before $X/D \sim 12$. For full blockage in **Figure 8** (e), the $< u'u' >$ profiles reach almost uniform distribution $3D$ after the porous block ($X/D = 13$) at Re=7200 and 14400. However, $< u'T' >$ profiles in **Figure 8** (g) show non-uniform wavy patterns in this region. Moreover, the peaks of $< u'u' >$ and $< u'T' >$ profiles (such as points A and B) in **Figure 8** (e, g) are due to an intense shear stress caused by penetration of a streamwise-oriented high-momentum flow into the wake region behind the porous block.

The similar time-averaged velocity profiles of the partial blockage in **Figure 8** (b) demonstrate the minor impact of the Re number on the velocity distributions in the wake region. The velocity and temperature profiles at $Y/D > 4.6$ inFigure **8** (b, d) approach unity and zero, respectively. This means that the cold flow above $Y/D \sim 4.6$ is not influenced by the interactions between the shear layer above the porous block and the wake region. This observation is also confirmed by $< u'u' >$ and $< u'T' >$ profiles in **Figure 8** (f, h). In **Figure 8** (h), the peaks of $< u'T' >$ profiles (marked by horizontal lines) indicate different flow physics: peaks at elevation A are due to the shear layer between the streamwise-oriented high-momentum flow (exiting from the porous block) and bottom wall; peaks at elevation B are due to the shear layer induced by the penetration of the streamwise-oriented high momentum flow into the wake region; peaks at elevation C are due to interactions between the shear layer (at the interface elevation) and wake region; and finally, peaks at elevation D refer to the shear layer generated by the development of turbulent boundary layer over the porous block.

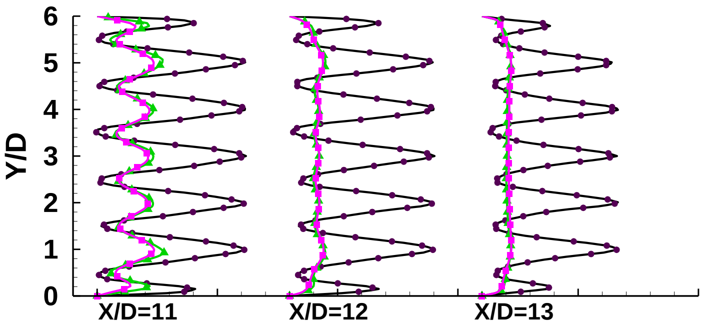

(a) Full blockage, $< \bar{u} >/U$

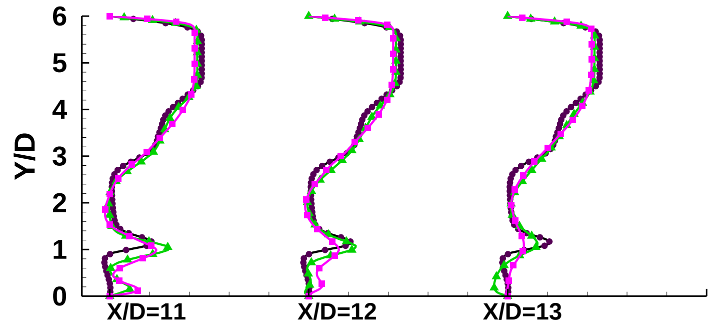

(b) Partial blockage, $< \bar{u} >/U$

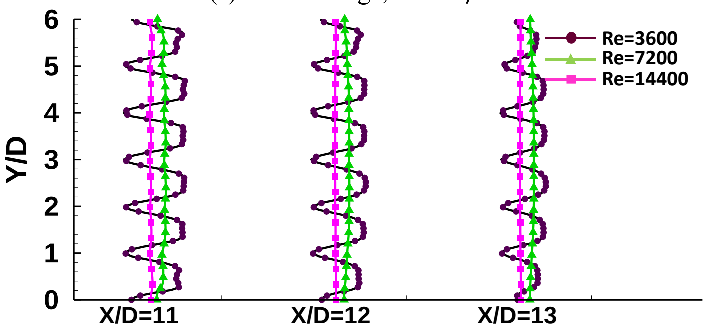

(c) Full blockage, $< \overline{\Theta} >$

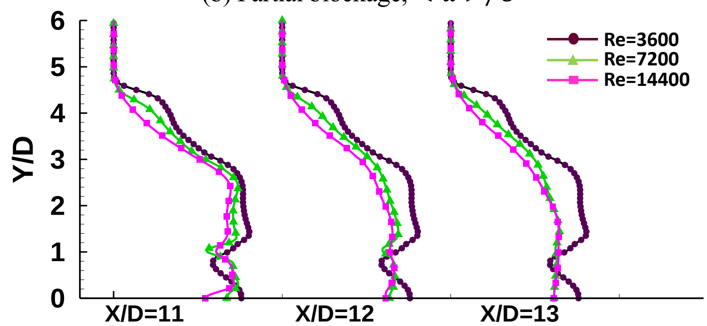

(d) Partial blockage, $< \overline{\Theta} >$

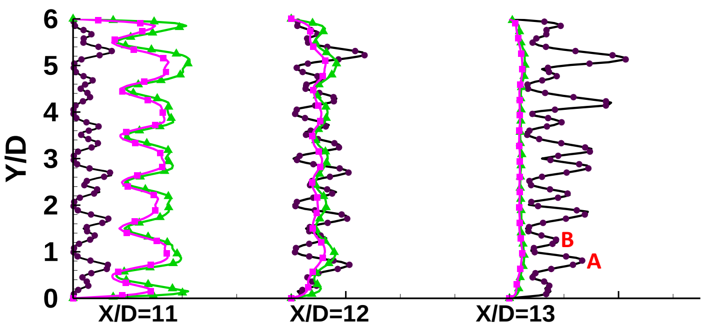

(e) Full blockage, $< u' u' >/UU$

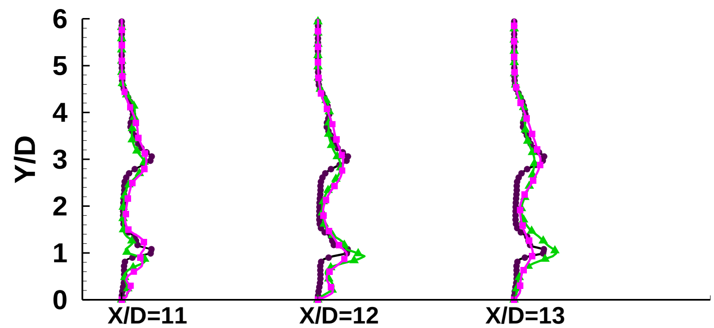

(f) Partial blockage, $< u' u' >/UU$

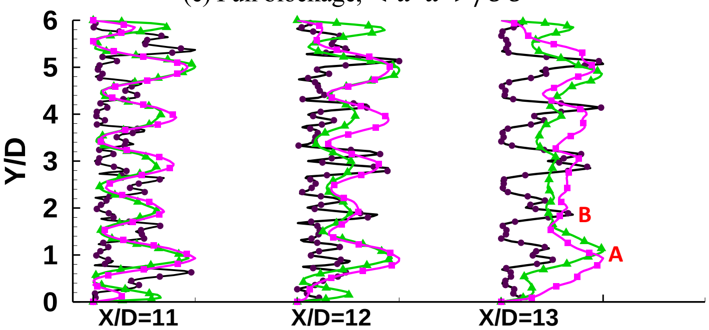

(g) Full blockage, $< u'T' >/< u'T' >_{max}$

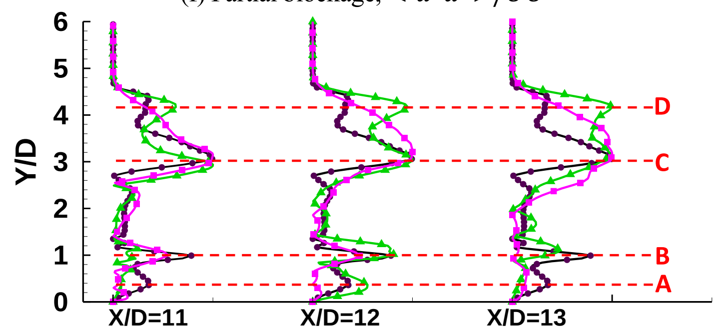

(h) Partial blockage, $< u'T' >/< u'T' >_{max}$

Figure 8 Vertical distribution of non-dimensional time-averaged streamwise velocity ($< \bar{u} >/U$), temperature ($< \bar{\Theta} >$), streamwise Reynolds shear stress ($< u' u' >/UU$) and streamwise turbulent heat flux ($< u'T' >/< u'T' >_{max}$) at different streamwise locations, $X/D = 11, 12,$ and 13 inside the wake region on the trough plane for three Re numbers 3600, 7200, and 14400; **Left**: Full blockage; **Right**: Partial blockage.

Figure 9 represents the contours of vertical turbulent heat flux on the crest and trough planes at Re=3600. In the wake region of full blockage stratified horizontal layers with minimum peaks (blue colour) and maximum peaks (red colour) are observed in the trough plane. The wavy pattern of stratified layers is associated with the channelling effect, as discussed in **Figure 8** (e, g). On the crest plane, minimum and maximum peaks can be observed near the bottom and top walls of the channel marked as A and B in **Figure 9** (a). These peaks are associated with the intense shear stresses near the walls. For the partial blockage, two distinct regions characterised by high-valued turbulent heat flux are identified. The first region with a significantly higher peak value initiates at $X/D = 4.9$ (Point A in **Figure 9** (d)) which corresponds to the onset of K-H instabilities and sudden increase in the turbulence production previously reported by the authors in [30]. In this region, the shear layer becomes unstable following flow separation at the leading edge, causing higher turbulent fluctuations that extend to the end of the porous block. At point A in **Figure 9** (d) and for Re=3600, the transition from a laminar to a turbulent boundary layer begins over the porous-fluid interface. By increasing the Re number from 3600 to 14400, the position of point A shifts upstream toward the leading edge. The second region of high-valued turbulent heat flux initiates at the trailing edge above the trailing face of the porous block. This region is induced by the upward transport of low-momentum flow in the wake region that interacts with the accelerated flow (see **Figure 6** (b)) above the wake region. Similar peaks in turbulent heat flux are observed on the crest plane of the partial blockage in **Figure 8** (h).

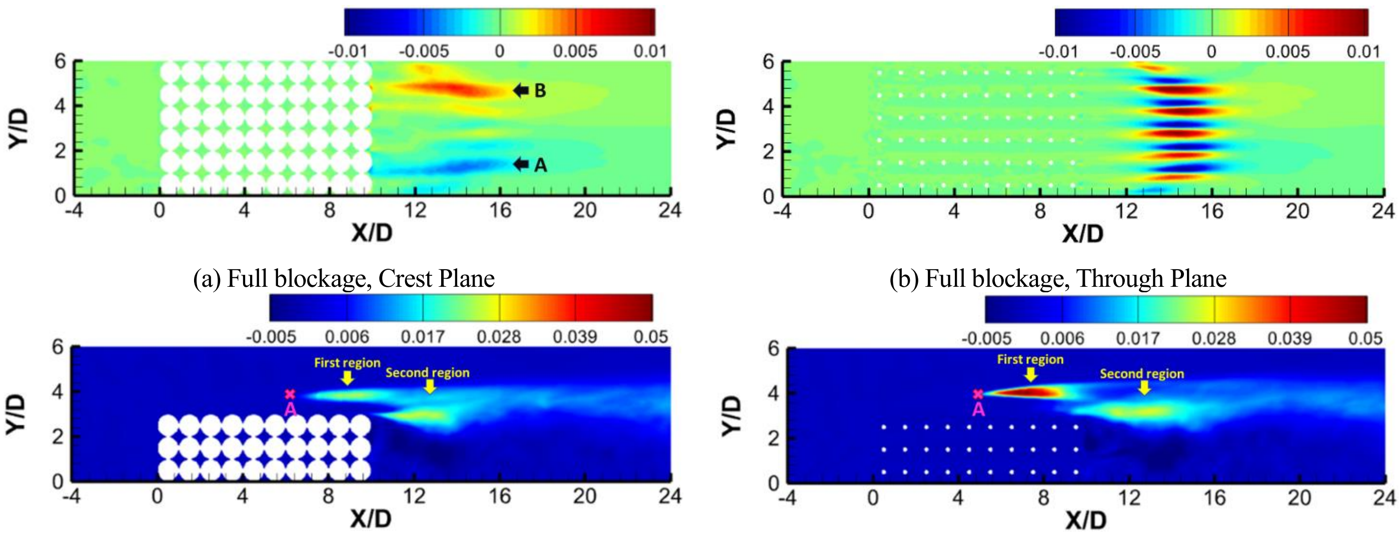

(a) Full blockage, Crest Plane (b) Full blockage, Through Plane

(c) Partial blockage, Crest Plane (d) Partial blockage, Through Plane

Figure 9 Front view contours of non-dimensional vertical turbulent heat flux on the crest and trough planes for Re=3600.

Figure 10 shows the time-averaged pressure coefficients (C_D) over the pore elements of full and partial blockages at Re=3600. The C_D contours illustrate how the partially filled porous structures change the magnitude and distribution of forces on the porous elements. Overall, the pressure coefficient decreases remarkably by moving downstream. For the full blockage, there is no visible difference between pore layers since the entire channel height is filled by the pore elements. As shown in **Figure 10** (a), the stagnation points on the spheres of the windward face occur right at the front of the spheres (called the position of symmetry). This means that the high-momentum incoming flow is exactly in the horizontal direction. The partial blockage in **Figure 10** (b) shows stagnation points at the front of the spheres (position of symmetry, where $\simeq 0$) for the second and third rows. The stagnation points in the first row, however, are shifted to the front bottom side with $\beta \simeq 225$. This deviation is attributed to the accelerated flow due to flow separation at the leading edge. The zoomed view in **Figure 7** (b) also shows this observation.

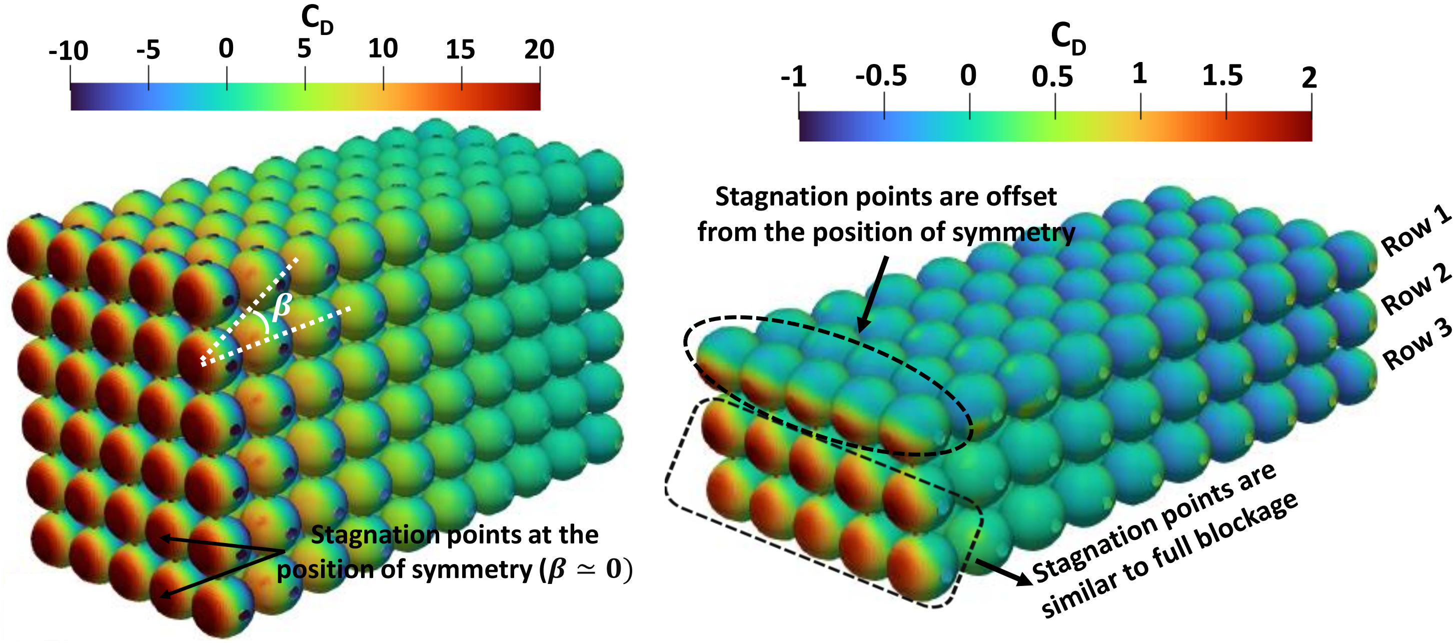

(a) Full blockage, Re=3600 (b) Partial blockage, Re=3600

Figure 10 Distribution of the time-averaged pressure coefficient ($C_D = (<\overline{p_X}> - p_{ref})/\rho U^2$) for full and partial blockages at Re=3600.

Table 3 lists the skin friction, pressure drag, lift forces, and their normalized values for full and partial blockages at three Re numbers. Since all cases are typically a kind of bluff body with flow separation, the pressure drag force (F_D) is the most dominant force. Both full and partial blockages experience an increase in the skin friction and pressure drag forces as the Re number rises. However, the full blockage is more affected by the Re number. For instance, increasing the Re number from 3600 to 14400 for the full blockage amplifies pressure drag and skin friction forces by nearly 20 and 9 times, respectively. While in the case of partial blockage, the corresponding values are nearly 14 and 7. Further, the full blockage produces at least 21 and 11 times more pressure drag and more skin friction forces than the partial blockage. For example, the pressure drag for the partial blockage is nearly 4.7% and 3.2% of the full blockage at Re=3600 and 14400, respectively. At these two Re numbers, the skin friction force of the partial blockage is 8.8% and 7.1% of the full blockage. Finally, the percentage change of the pressure drag defined as $PC_{drag} = \left((C_{D,full} - C_{D,partial})/C_{D,full}\right) \times 100$, is 95.3%, 96.1%, and 96.8% at Re=3600, 7200 and 14400, respectively.

Table 3 Skin friction and pressure coefficients for full and partial blockages at different Re numbers

	Full blockage, Re=3600	**Partial blockage, Re=3600**	**Full blockage, Re=7200**	**Partial blockage, Re=7200**	**Full blockage, Re=14400**	**Partial blockage, Re=14400**
$F_D = \sum_S <\bar{p}> dA_{\perp,X}$	2.21×10^{-2}	1.03×10^{-3}	9.95×10^{-2}	3.83×10^{-3}	4.64×10^{-1}	1.50×10^{-2}
$F_L = \sum_S <\bar{p}> dA_{\perp,Y}$	0	4.10×10^{-4}	-2.10×10^{-4}	1.48×10^{-3}	5.10×10^{-4}	5.91×10^{-3}
$F_{\tau X} = \sum_S <\overline{\tau_X}> dA_{\parallel}$	3.10×10^{-3}	2.70×10^{-4}	9.79×10^{-3}	7.50×10^{-4}	2.83×10^{-2}	2.01×10^{-3}
$F_{\tau Y} = \sum_S <\overline{\tau_Y}> dA_{\parallel}$	0	9.00×10^{-5}	6.00×10^{-6}	2.20×10^{-4}	5.70×10^{-5}	5.90×10^{-4}
$F_D/F_{D,partial}$	21.39	1.00	26.02	1.00	30.88	1.00
$F_L/F_{L,partial}$	0	1.00	-0.15	1.00	0.09	1.00
$F_{\tau X}/F_{\tau X,partial}$	11.41	1.00	13.07	1.00	14.09	1.00
$F_{\tau Y}/F_{\tau Y,partial}$	0	1.00	0.03	1.00	-0.10	1.00

Figure 11 displays contours of time-averaged Nu number on the pore elements for full and partial blockages at Re=3600. A significant reduction is observed in the Nu number by moving downstream. For full blockage, the maximum Nu number is nearly 20% higher than that for partial blockage. Also, **Figure 11** (a) notifies that the Nu number distribution is nearly uniform on the first column (windward face) of the porous block since the entire channel height is fully occupied by the pore elements. However, for the following columns, some regions with higher Nu values are identified on the upper and lower parts of the pore elements. These regions are attributed to the channelling effects, as discussed in **Figure 6** (a). Nu number contours for the partial blockage in **Figure 11** (b) illuminate a non-uniform distribution among porous layers (rows). Four regions with high-valued Nu numbers are detected in **Figure 11** (b). The peaks marked as "A" are associated with the flow acceleration due to the channelling effects. The peaks marked as "B" are associated with the accelerated flow due to flow separation at the leading edge (see the zoomed view in **Figure 7** (b)). The high-value regions near the porous-fluid interface, marked as "C", are due to the recirculation region between two successive pore elements as shown by zoomed streamlines in **Figure 11**

(b). Finally, areas with high magnitude Nu numbers on the lower sides of pore elements, marked as "D", correspond to the effect of flow leakage.

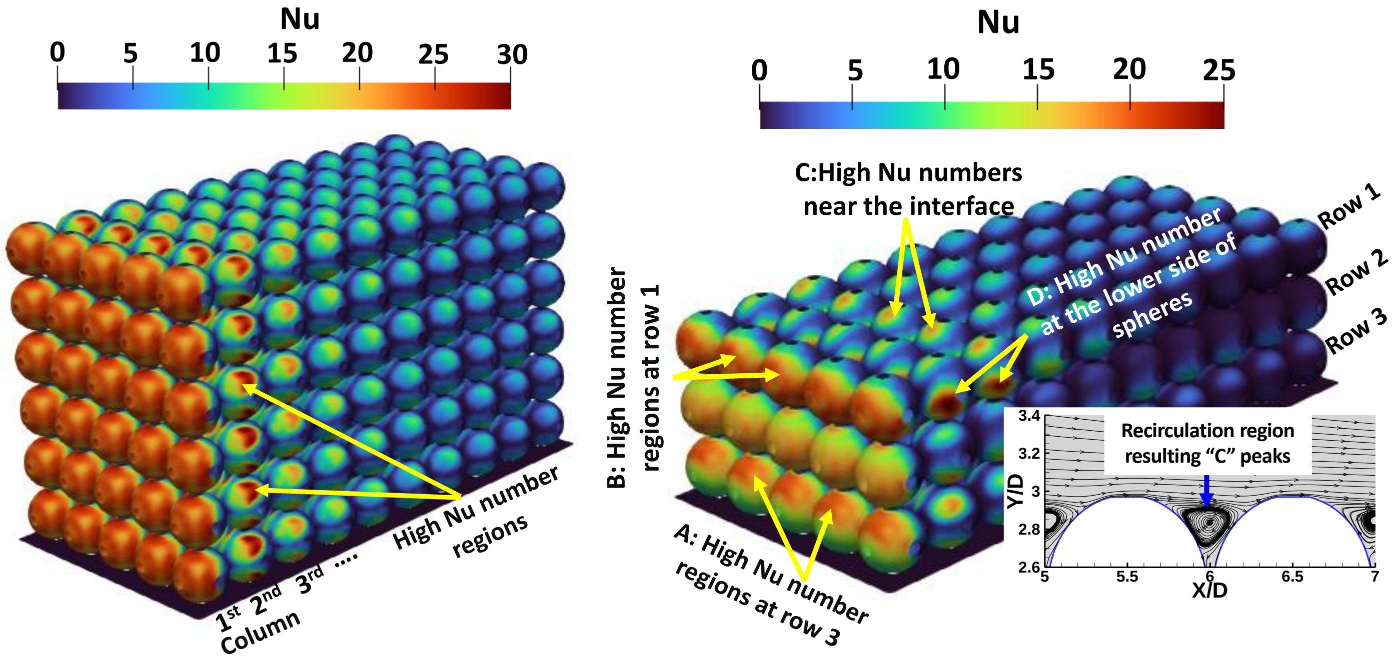

(a) Full blockage, Re=3600 (b) Partial blockage, Re=3600

Figure 11 Distribution of the time-averaged Nusselt number ($Nu = \frac{D}{(k_f[T_{wall}-T_{inlet}]A_s)} \iint_{A_s} q_{wall,loc} dA_s$ for full and partial blockages at Re=3600.

Figure 12 displays the time-averaged Nu number profiles along the porous length for the full and partial blockages at different Re numbers. The impact of the Re number is remarkable for each blockage ratio. At the leading edge, the Nu number of full blockage at Re=14400 is 2.1 times greater than that at Re=3600, and it increases to 4.7 times at the trailing edge. The same ratios are detected for partial blockage. At the leading edge, the Nu numbers of full blockage are nearly 36%, 34%, and 31% higher than those of partial blockage at Re numbers 3600, 7200, and 14400, respectively. The differences increase dramatically by moving downstream. The Nu numbers at the trailing edge of full blockage are 73%, 77%, and 72% greater than those of partial blockage at three Re numbers, correspondingly. Furthermore, the percentage change of the Nu number defined as $PC_{Nu} = \left(\left(Nu_{full} - Nu_{partial}\right)/Nu_{full}\right) \times 100$ is 51.2%, 58.2%, and 57.3% for Re=3600, 7200, and 14400, respectively. It can be inferred that the Nu number difference between the two blockage ratios is slightly affected by the Re number, and the average Nu number for the full blockage is at most 57.3% greater than that for the partial blockage. Tables in **Figure 12** indicate that Nu numbers can be estimated by a third-degree polynomial for all cases except full blockage at Re=14400, which varies linearly along the streamwise distance.

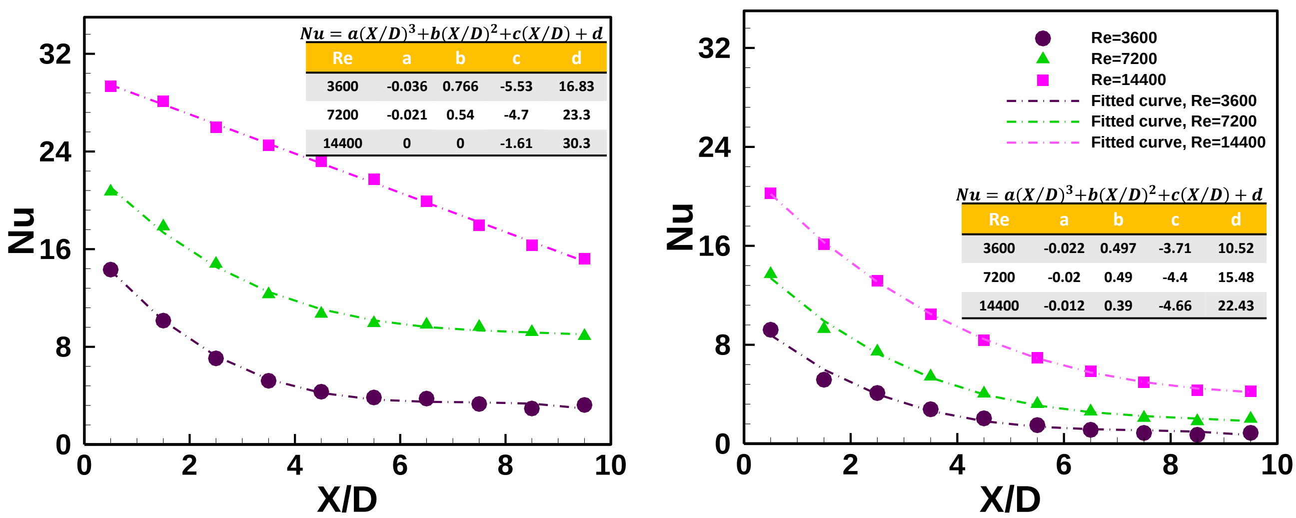

(a) Full blockage

(b) Partial blockage

Figure 12 Streamwise distribution of the time-averaged Nu number for full and partial blockages at three Re numbers, 3600, 7200, and 14400. Tables show the coefficients of third-degree polynomial correlation for representing the Nu distribution along the porous length.

Figure 13 displays the bar chart of Nu number over pore elements for two blockage ratios at three Re numbers. The Nu number of each pore element (sphere) for full blockage is generally greater than that for partial blockage, particularly for the spheres near the trailing edge (spheres 91-93, 101-103). For each blockage ratio, Nu number variations in the vertical/streamwise directions show similar patterns at different Re numbers.

For full blockage at Re=3600, the Nu number of sphere#11 is 4.8 times that of sphere#101, and this ratio is almost preserved for Nu numbers of spheres#13 and #103. At Re=14400, the ratio of Nu number between sphere#11 and sphere#101 drops to 1.9, similar to the ratio between sphere#13 and #103. Thus, the variation of the Nu number from the leading edge to the trailing edge is more severe for Re=3600 compared to Re=14400. **Figure 13** indicates that at the leading edge, the Nu number of full blockage is almost uniform along the vertical direction. For instance, the difference between the Nu numbers of spheres#11 and #13 is nearly 1.2% and 1.5% at Re=3600 and Re=14400, respectively. At the trailing edge, however, this difference (i.e., comparison of spheres#101 and #103) rises to 10.5% at Re=3600 and 2.73% at Re=14400. Therefore, it can be inferred that at higher Re numbers of the full blockage, the Nu number preserves its uniform distribution in the vertical direction at the trailing edge; however, at lower Re numbers, this trend is not observed.

For partial blockage, **Figure 13** informs two main notes about the Nu variations in the streamwise and vertical directions: 1) By moving downstream in the streamwise direction the Nu numbers of spheres#11 and #13 at Re= 3600 are approximately 10.3 and 13.9 times greater than spheres#101 and #103, respectively. At Re=14400, the Nu number ratio of spheres#11 to #101 is 4.7, which is also true for spheres#13 and #103. Therefore, as the Re number increases, the Nu number drops less in the streamwise direction by moving downstream; 2) At the first half of the porous length, the Nu number experiences a high growth in the vertical direction by approaching the porous-fluid interface. For instance, at the leading edge (1^{st} column), the Nu number of sphere#11 at Re=3600 and 14400 is 19.8% and 8.3% greater than that of sphere#13, respectively. Higher Nu numbers for the spheres near the interface at the leading edge are attributed to the high-speed angled flow due to flow separation (see "B" in **Figure 11** (b)). Also, the Nu number growth in the vertical direction for the 2^{nd}, 3^{rd}, and 4^{th} columns is 55%, 106%, and 69.6%, respectively, at Re=3600. The high Nu numbers for these columns are attributed to the local peaks marked as “C” and “D” in **Figure 11** (b). Whereas, at Re=14400, the Nu number growth for the 2nd, 3rd, and 4th columns is 22%, 69.6%, and 60%, respectively. Therefore, as the Re number rises, the Nu number growth in the vertical direction falls for the corresponding columns.

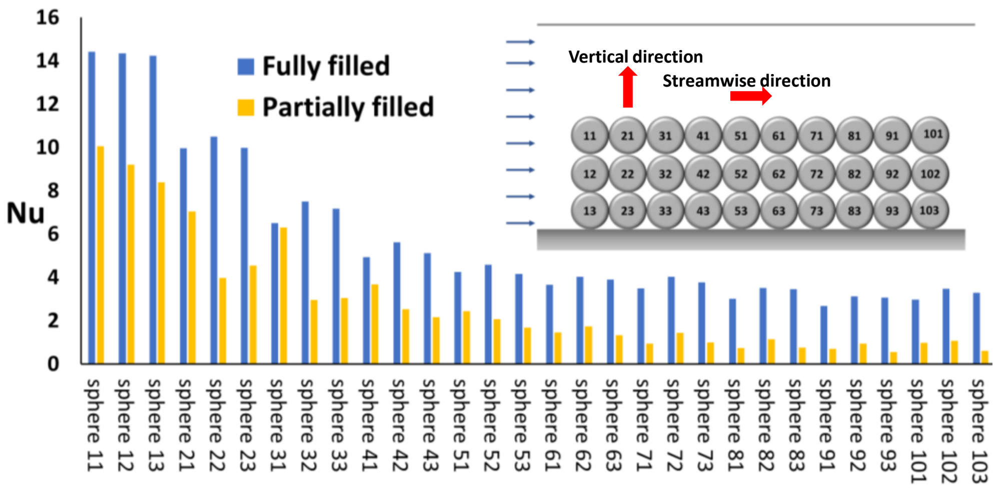

(a) Re=3600

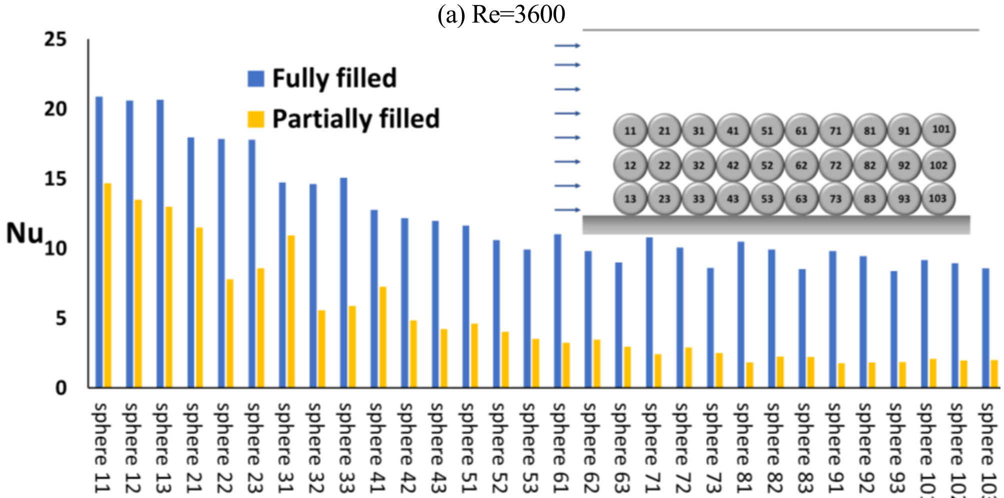

(b) Re=7200

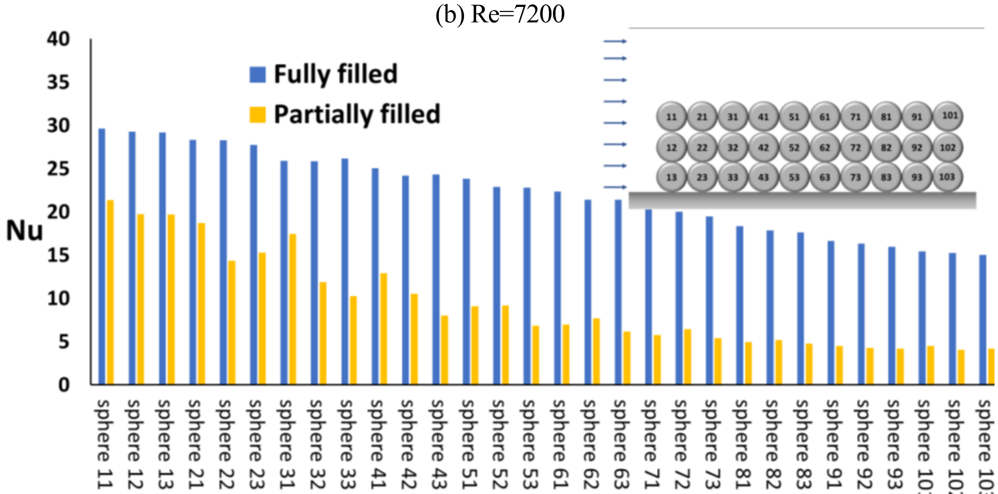

(c) Re=14400

Figure 13 Distribution of the time- and spatially-averaged Nusselt number over pore elements of the porous block for full and partial blockages at three Re numbers. Sphere "ij" indicates the sphere's location in the ith column and jth row of the porous block (e.g., sphere 63 means the 6th column in the porous block and above the bottom wall). The first row is located on the porous-fluid interface and the first column is located at the leading edge of the porous block.

To further investigate the impact of the flow leakage and channelling effect, streamlines and local distributions of the Nu number on sphere#21 are depicted in **Figure 14** (a, b) at Re=3600. For full blockage, high values (peaks) of the Nu number appear both in the upper and lower hemispheres, whereas partial blockage only shows peaks in the lower hemisphere. For full blockage, the streamlines (coloured by the streamwise velocity) are almost in the streamwise direction, indicating channelling effects on both the lower and upper hemispheres. The channelling effects lead to the appearance of local peaks in the Nu number distribution over the pore element (red-coloured areas in **Figure 14** (a)). For the partial blockage in **Figure 14** (b), the upward streamlines with high values of vertical velocity represent the flow leakage from the porous into non-porous regions. The flow leakage causes a significant increase in the local Nu number at the lower sides of the pore element.

The histogram of the Nu number on sphere#21 for the full and partial blockages in **Figure 14** (c, d) indicates that nearly 51% and 66% of the grid cells contain a Nu number between 0.64 to 5.8, respectively. This means that the Nu number distributions of full and partial blockages do not differ significantly in the majority of grid cells. Nevertheless, for the full blockage, nearly 43% of the cells contain a Nu number between 7 to 25, while it is 34% for the partial blockage. In addition, the histograms show that there is no grid cell containing $Nu > 25$ for partial blockage, whereas 6% of grid cells possess $25 < Nu < 32$ for the full blockage. As can be seen in **Figure 13** (a), the spatially-averaged Nu number of full blockage for sphere#21 is nearly 29% higher than that of partial blockage. A comparison of full and partial blockages' histograms in **Figure 14** (c, d) explains the reason for the difference in Nu number of sphere#21 for two blockage ratios in **Figure 13** (a).

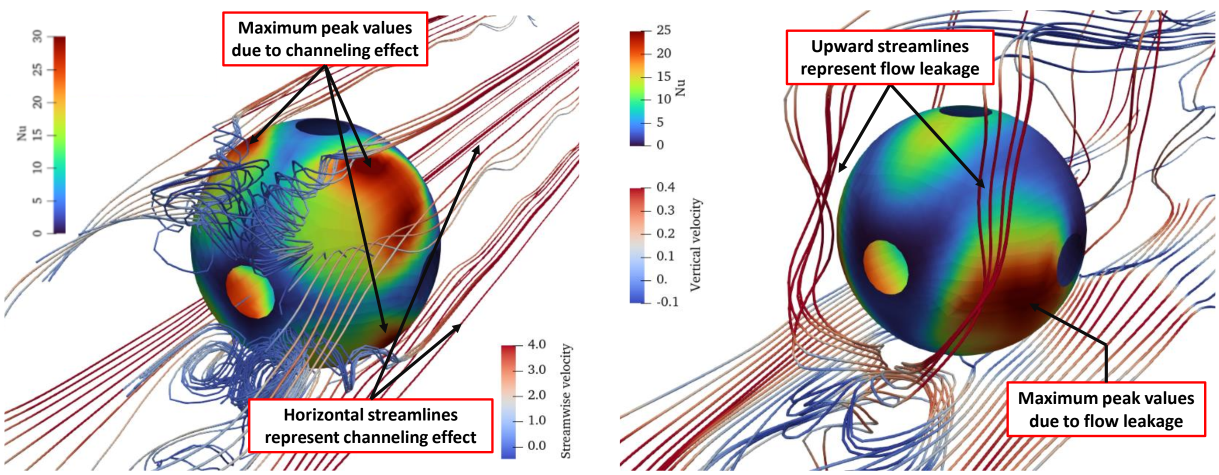

(a) Contour of Nu number on sphere 21 (Full blockage) (b) Contour of Nu number on sphere 21 (Partial blockage)

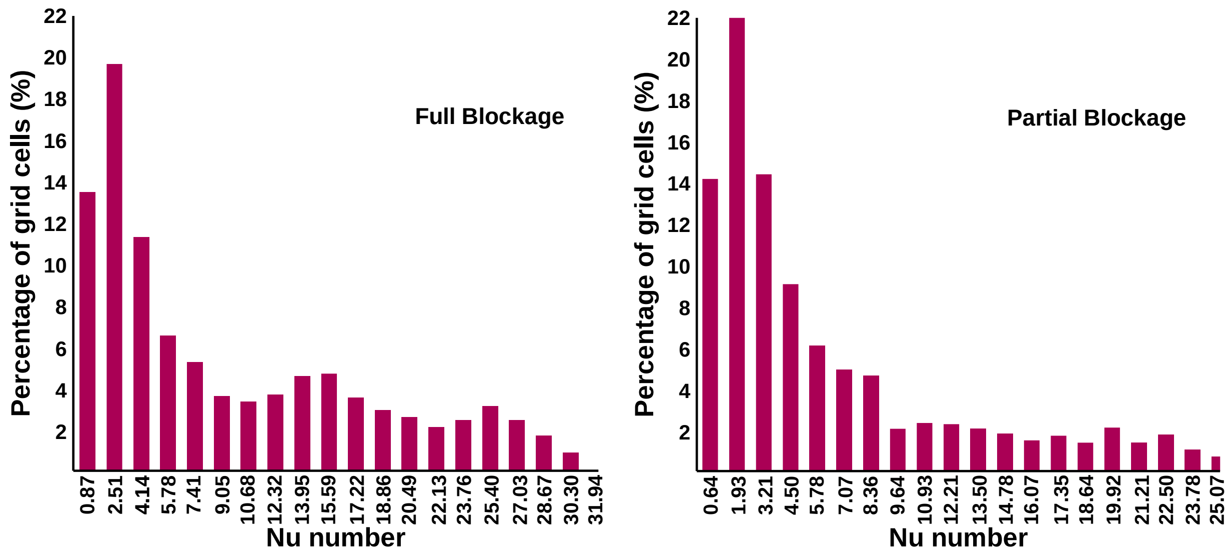

c) Histogram of Nu number on sphere 21 for full blockage

d) Histogram of Nu number on sphere 21 for partial blockage

Figure 14 The impact of the flow leakage and channelling effects on the distribution of Nusselt number over the pore elements (sphere 21) of the full blockage and partial blockage cases at Re=3600.

4 Conclusion

This paper presents pore-scale large eddy simulations (LES) for two different packed bed energy storage systems (PBESSs), namely full blockage and partial blockage at three Re numbers, 3600, 7200 and 14400. The main objective was to investigate the effect of partially blocking and Re number on the flow leakage and channelling effect that strongly modify local Nu number and pressure drop distributions in PBESSs. To this end, wake flow features, flow leakage, channelling effect, and energy exchange between the porous and non-porous regions are examined under the discharge process which have not been studied in the literature yet. The results are presented by deploying first- and second-order statistics of velocity and temperature, turbulent heat flux, as well as distributions of pressure drag and Nu number over the pore elements. The major findings are summarized as follows:

1) For both PBESSs, the channelling effect dominates the flow pattern inside the porous region, generating streamwise-oriented high momentum paths. It causes non-uniform wavy temperature distributions inside the porous block and local maximum peaks of Nu number on the upper and lower sides of the pore elements. By moving downstream, the wavy trend weakens significantly, particularly at Re=7200 and 14400.
2) As the Re number increases, the temperature profiles of partial blockage are less affected compared to those of full blockage. Temperature profiles of partial blockage indicate that 1.47D above the porous-fluid interface, the incoming cold flow does not interact with the hot pore elements.
3) For partial blockage, 79% and 65% of the flow entering the porous block leaks from the porous-fluid interface through the entire and first half of the porous length, respectively, at Re=3600. As the Re number increases from 3600 to 14400, the flow leakage reduces by 26%. Moreover, the flow leakage affects the Nu number distribution over the pore elements and causes local maximum peaks of the Nu number at the lower sides of pore elements. It also changes the position of the stagnation points at the leading edge of the porous block near the porous-fluid interface, and shifts them to the lower side of the spheres.
4) For partial blockage, the flow leakage leads to counter-rotating vortex pair (CRVP) flow structures over the porous block, originating from the porous inside. CRVPs over the interface manipulate the

momentum and energy exchange between the porous and non-porous regions. The temperature distributions above the porous block follow the velocity patterns induced by the CRVP structures.

5) For partial blockages, the pressure drag is 4.7% and 3.2% of the full blockage at Re=3600 and Re=14400, respectively. For the full blockage, as the Re number increases from 3600 to 14400, the pressure drag and skin friction forces amplify by nearly 20.3 and 9.1 times, respectively. While, for the partial blockage, the corresponding values are 14.4 and 7.3.
6) In general, the average Nu number for the full blockage is at most 57.3% higher than that for the partial blockage. Increasing the Re number from 3600 to 14400 leads to at least 210% growth in the Nu number for both blockage ratios. Based on local Nu number distributions for partial blockage, as the Re number increases the Nu number reduces less in the streamwise direction and grows less in the vertical direction toward the porous-fluid interface. The results demonstrate that the local streamwise distributions of the Nu number follow a third-degree polynomial.
7) Overall comparison of the full and partial blockages in this study shows that the percentage change of the pressure drop is 95%, whereas the percentage change of the average Nu number is at most 57.3%. Accordingly, full blocking of the available fluid flow area is not necessarily the best design since it can result in unnecessary higher pressure drops without considerable heat transfer improvements.

The model and hence the results presented in this work can be extended to a more realistic scenario under which PBESSs operate. Three categories for the future direction can be outlined in the followings:

1. Time-dependent inflow boundary condition (more practical application): Since PBESSs operate under a transient heating input (charge) and output (discharge), their actual performance needs to be studied in a time-dependent inflow condition. The present paper focuses on the discharge phase at three different Re numbers using constant inflow boundary conditions. In the next phase of this project, the transient behaviour of the PBESS in both the charge and discharge phases will be simulated.
2. Conjugate heat transfer between the solid and fluid phases within the porous region (more accurate modelling): In the present study it was assumed that the temperature of the pore elements is constant with Dirichlet boundary condition. However, to predict the heat transfer characteristics more accurately, it is recommended to solve for energy equation in the solid region. Thus, a coupled boundary condition between the solid phase and fluid flow around it can be implemented, using conjugate heat transfer modelling.
3. Modelling porous elements using randomly packed porous media (more realistic geometry): The porous block in this study is a cubic arrangement of uniform spheres with a constant porosity. For a more realistic prediction of flow and thermal features in a thermal energy storage system, a randomly packed bed needs to be investigated, and to identify the influence of packed bed randomness on the physics of flow leakage, chanelling effect and wake flow.

Acknowledgement

This work was supported by the UK Engineering and Physical Sciences Research Council (EPSRC) [grant numbers EP/T012242/1 and EP/T012242/2]. Data supporting this publication can be obtained on request. The authors would like to acknowledge the assistance given by Research IT and the use of the Computational Shared Facility at The University of Manchester.

References

[1] E. Barbour, D. Mignard, Y. Ding, and Y. Li, "Adiabatic compressed air energy storage with packed bed thermal energy storage," *Applied Energy*, vol. 155, pp. 804-815, 2015, doi: https://doi.org/10.1016/j.apenergy.2015.06.019.

[2] R. Morgan, S. Nelmes, E. Gibson, and G. Brett, "Liquid air energy storage–analysis and first results from a pilot scale demonstration plant," *Applied Energy*, vol. 137, pp. 845-853, 2015, doi: https://doi.org/10.1016/j.apenergy.2014.07.109.

[3] A. White, G. Parks, and C. N. Markides, "Thermodynamic analysis of pumped thermal electricity storage," *Applied Thermal Engineering*, vol. 53, no. 2, pp. 291-298, 2013/05/02/ 2013, doi: https://doi.org/10.1016/j.applthermaleng.2012.03.030.

[4] J. D. McTigue, C. N. Markides, and A. J. White, "Performance response of packed-bed thermal storage to cycle duration perturbations," *Journal of Energy Storage*, vol. 19, pp. 379-392, 2018/10/01/ 2018, doi: https://doi.org/10.1016/j.est.2018.08.016.

[5] A. Gautam and R. Saini, "A review on technical, applications and economic aspect of packed bed solar thermal energy storage system," *Journal of Energy Storage*, vol. 27, p. 101046, 2020, doi: https://doi.org/10.1016/j.est.2019.101046.

[6] Y. Mahmoudi, K. Hooman, and K. Vafai, *Convective Heat Transfer in Porous Media*. , 1st ed., CRC Press, Boca Raton, 2019.

[7] M. Khaljani, M. Nazari, M. Azarpeyvand, and Y. Mahmoudi, "Experimental and Pore-Scale Analysis of Flow and Thermal Fields in a Packed Bed Channel," *Heat Transfer Engineering*, vol. 43, no. 13, pp. 1119-1134, 2022, doi: https://doi-org.manchester.idm.oclc.org/10.1080/01457632.2021.1943846

[8] R. A. Lawag and H. M. Ali, "Phase change materials for thermal management and energy storage: A review," *Journal of Energy Storage*, vol. 55, p. 105602, 2022, doi: https://doi.org/10.1016/j.est.2022.105602.

[9] F. Selimefendigil and H. F. Öztop, "Impacts of using an elastic fin on the phase change process under magnetic field during hybrid nanoliquid convection through a PCM-packed bed system," *International Journal of Mechanical Sciences*, vol. 216, p. 106958, 2022, doi: https://doi.org/10.1016/j.ijmecsci.2021.106958.

[10] C. Zhao, M. Opolot, M. Liu, F. Bruno, S. Mancin, and K. Hooman, "Numerical study of melting performance enhancement for PCM in an annular enclosure with internal-external fins and metal foams," *International Journal of Heat and Mass Transfer*, vol. 150, p. 119348, 2020, doi: https://doi.org/10.1016/j.ijheatmasstransfer.2020.119348.

[11] F. Selimefendigil and H. F. Öztop, "Effects of flow separation and shape factor of nanoparticles in heat transfer fluid for convection thorough phase change material (PCM) installed cylinder for energy technology applications," *Journal of Energy Storage*, vol. 41, p. 102945, 2021, doi: https://doi.org/10.1016/j.est.2021.102945.

[12] L. Kolsi, F. Selimefendigil, M. Omri, and L. Ladhar, "Combined Effects of Sequential Velocity and Variable Magnetic Field on the Phase Change Process in a 3D Cylinder Having a Conic-Shaped PCM-Packed Bed System," *Mathematics*, vol. 9, no. 23, p. 3019, 2021, doi: 10.3390/math9233019.

[13] B. Baghapour, M. Rouhani, A. Sharafian, S. B. Kalhori, and M. Bahrami, "A pressure drop study for packed bed adsorption thermal energy storage," *Applied Thermal Engineering*, vol. 138, pp. 731-739, 2018, doi: https://doi.org/10.1016/j.applthermaleng.2018.03.098.

[14] K. Hooman, "Thermohydraulics of Porous Heat Exchangers: Full or Partial Blockage?," in *5th International Conference on Porous Media and Their Applications in Science, Engineering and Industry*., K. Vafai., A. Bejan., A. Nakayama., and O. Manca., Eds., 2014, in ECI Symposium Series,, doi: https://dc.engconfintl.org/porous_media_V/19.

[15] M. El-Kassaby and A. Ghoneim, "Comparison of measured and predicted performance of different heat storage systems," *Renewable Energy,* vol. 3, no. 8, pp. 849-856, 1993, doi: https://doi.org/10.1016/0960-1481(93)90041-E.

[16] J. E. Pacheco, S. K. Showalter, and W. J. Kolb, "Development of a molten-salt thermocline thermal storage system for parabolic trough plants," *Journal of Solar Energy Engineering,* vol. 124, no. 2, pp. 153-159, 2002., doi: https://doi.org/10.1115/1.1464123.

[17] X. Yang, X. Yang, F. G. Qin, and R. Jiang, "Experimental investigation of a molten salt thermocline storage tank," *International Journal of Sustainable Energy,* vol. 35, no. 6, pp. 606-614, 2016, doi: 10.1080/14786451.2014.930465

[18] M. S. Hossain and B. Shabani, "Air flow through confined metal foam passage: Experimental investigation and mathematical modelling," *Experimental Thermal and Fluid Science,* vol. 99, pp. 13-25, 2018, doi: https://doi.org/10.1016/j.expthermflusci.2018.07.018.

[19] F. Shikh Anuar, I. Ashtiani Abdi, M. Odabaee, and K. Hooman, "Experimental study of fluid flow behaviour and pressure drop in channels partially filled with metal foams," *Experimental Thermal and Fluid Science,* vol. 99, pp. 117-128, 2018/12/01/ 2018, doi: https://doi.org/10.1016/j.expthermflusci.2018.07.032.

[20] R. Singh, R. Saini, and J. Saini, "Nusselt number and friction factor correlations for packed bed solar energy storage system having large sized elements of different shapes," *Solar Energy,* vol. 80, no. 7, pp. 760-771, 2006, doi: https://doi.org/10.1016/j.solener.2005.07.001.

[21] F. S. Anuar, I. A. Abdi, and K. Hooman, "Flow visualization study of partially filled channel with aluminium foam block," *International Journal of Heat and Mass Transfer,* vol. 127, pp. 1197-1211, 2018, doi: https://doi.org/10.1016/j.ijheatmasstransfer.2018.07.047.

[22] F. S. Anuar, K. Hooman, M. R. Malayeri, and I. A. Abdi, "Experimental study of particulate fouling in partially filled channel with open-cell metal foam," *Experimental Thermal and Fluid Science,* vol. 110, p. 109941, 2020, doi: https://doi.org/10.1016/j.expthermflusci.2019.109941.

[23] Z. Chang, X. Li, C. Xu, C. Chang, and Z. Wang, "The design and numerical study of a 2MWh molten salt thermocline tank," *Energy Procedia,* vol. 69, pp. 779-789, 2015, doi: https://doi.org/10.1016/j.egypro.2015.03.094.

[24] Z. Yang and S. V. Garimella, "Molten-salt thermal energy storage in thermoclines under different environmental boundary conditions," *Applied Energy,* vol. 87, no. 11, pp. 3322-3329, 2010, doi: https://doi.org/10.1016/j.apenergy.2010.04.024.

[25] R. Habib, N. Karimi, B. Yadollahi, M. H. Doranehgard, and L. K. Li, "A pore-scale assessment of the dynamic response of forced convection in porous media to inlet flow modulations," *International Journal of Heat and Mass Transfer,* vol. 153, p. 119657, 2020, doi: https://doi.org/10.1016/j.ijheatmasstransfer.2020.119657.

[26] F. Selimefendigil and H. F. Öztop, "Impacts of magnetic field and hybrid nanoparticles in the heat transfer fluid on the thermal performance of phase change material installed energy storage system and predictive modeling with artificial neural networks," *Journal of Energy Storage,* vol. 32, p. 101793, 2020, doi: https://doi.org/10.1016/j.est.2020.101793.

[27] J. Yang, Q. Wang, M. Zeng, and A. Nakayama, "Computational study of forced convective heat transfer in structured packed beds with spherical or ellipsoidal particles," *Chemical Engineering Science,* vol. 65, no. 2, pp. 726-738, 2010, doi: https://doi.org/10.1016/j.ces.2009.09.026

[28] Y. Mahmoudi and N. Karimi, "Numerical investigation of heat transfer enhancement in a pipe partially filled with a porous material under local thermal non-equilibrium condition," *International*

Journal of Heat and Mass Transfer, vol. 68, pp. 161-173, 2014, doi: https://doi.org/10.1016/j.ijheatmasstransfer.2013.09.020.

[29] X. Chu, G. Yang, S. Pandey, and B. Weigand, "Direct numerical simulation of convective heat transfer in porous media," *International Journal of Heat and Mass Transfer*, vol. 133, pp. 11-20, 2019, doi: https://doi.org/10.1016/j.ijheatmasstransfer.2018.11.172.

[30] M. Jadidi, A. Revell, and Y. Mahmoudi, "Pore-scale Large Eddy Simulation of Turbulent Flow and Heat Transfer over Porous Media," *Applied Thermal Engineering*, p. 118916, 2022, doi: https://doi.org/10.1016/j.applthermaleng.2022.118916

[31] M. Jadidi, H. K. Param, A. Revell, and Y. Mahmoudi, "Flow leakage and Kelvin–Helmholtz instability of turbulent flow over porous media," *Physics of Fluids*, vol. 34, no. 10, p. 105114, 2022, doi: 10.1063/5.0111195.

[32] S. B. Pope and S. B. Pope, *Turbulent flows*. Cambridge university press, 2000.

[33] P. Sagaut, *Large eddy simulation for incompressible flows: an introduction*. Springer Science & Business Media, 2006.

[34] W.-W. Kim, S. Menon, W.-W. Kim, and S. Menon, "Application of the localized dynamic subgrid-scale model to turbulent wall-bounded flows," in *35th Aerospace Sciences Meeting and Exhibit*, 1997, p. 210, doi: https://doi-org.manchester.idm.oclc.org/10.2514/6.1997-210.

[35] W. M. Kays, "Turbulent Prandtl number. Where are we?," *ASME Journal of Heat Transfer*, vol. 116, no. 2, pp. 284-295, 1994.

[36] H. Jasak, A. Jemcov, and Z. Tukovic, "OpenFOAM: A C++ library for complex physics simulations," in *International Workshop on Coupled Methods in Numerical Dynamics*, 2007, vol. 1000: IUC Dubrovnik Croatia, pp. 1-20.

[37] C. Greenshields and H. Weller, "Notes on computational fluid dynamics: General principles," *CFD Direct Ltd.: Reading, UK*, 2022.

[38] F. Bazdidi-Tehrani, A. Ghafouri, and M. Jadidi, "Grid resolution assessment in large eddy simulation of dispersion around an isolated cubic building," *Journal of Wind Engineering and Industrial Aerodynamics*, vol. 121, pp. 1-15, 201, doi: https://doi.org/10.1016/j.jweia.2013.07.003

[39] L. Davidson, "How to estimate the resolution of an LES of recirculating flow," in *Quality and Reliability of Large-Eddy Simulations II*: Springer, 2011, pp. 269-286.

[40] J.-M. Leu, H.-C. Chan, and M. Chu, "Comparison of turbulent flow over solid and porous structures mounted on the bottom of a rectangular channel," *Flow Measurement and Instrumentation*, vol. 19, no. 6, pp. 331-337, 2008, doi: https://doi.org/10.1016/j.flowmeasinst.2008.05.001.

[41] J. S. Lee and K. Ogawa, "Pressure Drop Though Packed Bed," *Journal of Chemical Engineering of Japan*, vol. 27, no. 5, pp. 691-693, 1994., doi: 10.1252/jcej.27.691.

[42] S. Ergun, “Fluid Flow through Packed Columns,” Journal of Chemical Engineering Progress, Vol. 48, No. 2, pp. 89-94, 1952.

[43] M. Nazari, D. Jalali Vahid, R. K. Saray, and Y. Mahmoudi, "Experimental investigation of heat transfer and second law analysis in a pebble bed channel with internal heat generation," *International Journal of Heat and Mass Transfer*, vol. 114, pp. 688-702, 2017/11/01/ 2017, doi: https://doi.org/10.1016/j.ijheatmasstransfer.2017.06.079.

[44] K.Vafai, A. Bejan, W. J. Minkowycz, K. Khanafer, A Critical synthesis of pertinent models for turbulent transport through porous media, Advances in Numerical Heat Transfer, Vol. 2, Chapter 12, pp. 389–416, John Wiley & Sons, Hoboken, NJ, 2006.

[45] R.B. Bird, W.E. Stewart, E.N. Lightfoot, Transport Phenomena, 1st ed., John Wiley & Sons, New York, 1960.

[46] W.M. Kays, A.L. London, Compact Heat Exchangers., 3th ed., McGraw-Hill, New York,1984.

[47] T. L. Bergman, A. S. Lavine, F. P. Incropera, and D. P. DeWitt, *Introduction to Heat Transfer*. John Wiley & Sons, 2011.

[48] F. Kuwahara, M. Shirota, and A. Nakayama, "A numerical study of interfacial convective heat transfer coefficient in two-energy equation model for convection in porous media," *International Journal of Heat and Mass Transfer*, vol. 44, no. 6, pp. 1153-1159, 2001, doi: https://doi.org/10.1016/S0017-9310(00)00166-6

[49] X. Nie, R. Evitts, R. Besant, and J. Bolster, "A new technique to determine convection coefficients with flow through particle beds," *Journal of Heat Transfer*, vol. 133, no. 4, 2011, doi: https://doi-org.manchester.idm.oclc.org/10.1115/1.4002945.

[50] M. Nazari, D. J. Vahid, R. K. Saray, and Y. Mahmoudi, "Experimental investigation of heat transfer and second law analysis in a pebble bed channel with internal heat generation," *International Journal of Heat and Mass Transfer,* vol. 114, pp. 688-702, 2017, doi: https://doi.org/10.1016/j.ijheatmasstransfer.2017.06.079.

[51] B. Cabral and L. C. Leedom, "Imaging vector fields using line integral convolution," in *Proceedings of the 20th Annual Conference on Computer Graphics and Interactive Techniques*, 1993, pp. 263-270.